Instantaneous and Mean Compositional Structure of Bluff-Body Stabilized Nonpremixed Flames

B. B. DALLY* and A. R. MASRI
Department of Mechanical and Mechatronic Engineering, The University of Sydney, Sydney NSW, Australia

and

R. S. BARLOW and G. J. FIECHTNER
Combustion Research Facility, Sandia National Laboratories, Livermore, CA

Turbulent nonpremixed flames stabilized on an axisymmetric bluff-body burner are studied with fuels ranging from simple H_2/CO to complex H_2/CH_4 and gaseous methanol. The fuel-jet velocity is varied to investigate the Damköhler number effects on gas emissions, localized extinction (LE) in the neck zone, and the structure of the recirculation zone dependency on the flow field. Simultaneous, single-point measurements of temperature, major species, OH, and NO are made using the Raman/Rayleigh/Laser induced fluorescence (LIF) technique. The data are collected at different axial and radial locations along the full length of most flames and are presented in the form of ensemble means, root-mean-square (rms) fluctuations, scatter plots, and probability density functions (PDF). It is found that up to three mixing layers may exist in the recirculation zone, one on the air side of the outer vortex, one between the inner and the outer vortices, and one between the fuel jet and the inner vortex. With increasing jet momentum flux, the average mixture in the outer vortex loses its strength and the stoichiometric contour shifts closer to the fuel jet. The decay rate of the mixture fraction on the centerline exhibits similar trends to the ordinary jet flame downstream of the recirculation zone whereas different trends are found inside the recirculation zone. The laminar flame computations with constant mass diffusivities and Lewis number (Le) = 1 are found to be better guides for the measured temperature and stable species mass fraction in the turbulent flames. The measured peak mass fractions of CO and H_2 are similar to those reported earlier for pilot-stabilized flames of similar fuels. Compared with laminar flame compositions with equal diffusivities and Le = 1.0, measured CO may be in superflamelet concentration. Hydroxyl radical **and** H_2 are found **not** to be in superflamelet levels contrary to earlier findings in piloted flames. The start of LE and the bimodality of the conditional PDF are consistent with those reported earlier for piloted flames of similar fuels.

NOMENCLATURE

a	stretch rate (1/s)
b_i	reactedness of species i
B_i	bimodality factor for species i
$\bar{B}_i$	mean bimodality factor for species i
% BO	percentage ratio of jet velocity over the blow-off velocity
D_B	bluff-body diameter (mm)
D_J	fuel-jet diameter (mm)
CMC	conditional moment closure
k_i	kurtosis of PDF calculated for species i
l_p	length of measurement probe volume (mm)
L_θ	scalar microscale (mm)
L_u	integral length scale (mm)
Le	Lewis number
LE	localized extinction
$\dot{M}_J$	momentum flux of the jet (N)
$n_{b_{x,y}}$	number of samples where scalar b is between x and y
N	total number of samples
P_i	mass fraction of species i
P_F	mass fraction at the frozen limit
P_L	mass fraction at the fully burnt limit
PDF	probability density function
r	radial distance from centerline (mm)
R_B	bluff-body radius (mm)
Re_t	turbulence Reynolds number
Re_J	jet Reynolds number
s_i	skewness of PDF calculated for species i
T'	rms fluctuation of the temperature
$\bar{T}$	mean temperature (K)
T_{IN}	temperature of the fuel at the jet exit plane (K)
T_{ad}	adiabatic flame temperature (K)

*Corresponding author.

COMBUSTION AND FLAME 114:119–148 (1998)

Published by Elsevier Science Inc.

0010-2180/98/$19.00
PII S0010-2180(97)00280-0

u' rms fluctuation of the velocity
U_{CO} coflow-air velocity (m/s)
U_{BO} fuel-jet velocity at extinction (m/s)
U_J fuel-jet velocity (m/s)
W_i atomic mass of element i
X distance above burner (mm)
Y_i mass fraction of species i
$\bar{Y}_i$ mean mass fraction of species i
Z_i conserved scalar of element i

Greek Symbols

$\Delta\xi_R$ width of the reaction zone
$\Delta b_{x,y}$ width of the scalar b interval bounded by x and y
λ wavelength (nm)
θ reactive scalar
ν kinematic viscosity (m^2/s)
ρ_J density of the fuel (kg/m^3)
ρ_{CO} density of the air coflow (kg/m^3)
ξ' rms fluctuation of mixture fraction
$\bar{\xi}$ mean mixture fraction
$\bar{\xi}_{cl}$ mean centerline mixture fraction
ξ_s stoichiometric mixture fraction
$\bar{\xi}_{vo}$ mean mixture fraction of the outer vortex

INTRODUCTION

This publication is aimed at providing a somewhat complete and quantitative understanding of the structure of bluff-body stabilized flames. The flames studied here are not unlike those found in practical combustors; yet they are nonsooting to facilitate laser diagnostics and have simple, well-defined boundary conditions for ease of modeling. Measurements of temperature, composition as well as formation, and emission of pollutants have been made for a range of flame conditions with various fuel mixtures. Only samples of the available data are presented in this paper. The complete data set may be accessed on the worldwide web [1].

Understanding of combustion processes has advanced significantly in recent years such that the numerical simulation of practical combustors is closer to reality in many respects. Detailed chemical kinetic models, including the chemistry of some pollutants, have been developed for many fuels [2–5]. The systematic reduction of these mechanisms to levels manageable by current computer capabilities is now a well-established science [6, 7]. Many computational approaches are now potentially capable of simulating the structure of turbulent flames using enough details in the chemistry to account for finite-rate effects and for the formation of pollutants [8–11]. Progress in modeling has been paralleled by outstanding advances in combustion diagnostic methods that have resulted in a comprehensive bank of data for turbulent pilot-stabilized jet flames with parabolic (streaming) flows [12]. These data are now established benchmarks for the development and validation of combustion models. Interest in modeling, as well as experimentation, is now shifting to more complex flows, which better represent those of practical combustors, and a bank of data must be developed for such flows.

Bluff-body stabilized flows are, therefore, receiving significant attention because of their relevance to many engineering applications. The bluff-body burner studied here is an interesting model problem for industrial flows because of its simple and well-defined initial and boundary conditions, as well as its ability to stabilize flames with complex recirculating zones. It also provides a controlled medium where the interaction between chemistry and turbulence may be investigated. This region is located downstream of the recirculation zone (neck zone) where the turbulent mixing rate may become significant and flame blow-off occurs at sufficiently high flow velocities.

Roquemore et al. [13, 14] have identified two types of bluff-body stabilized flames: fuel-jet dominant and coflow-air dominant. The occurrences of these depend on the fuel jet and coflow-air velocities as well as the ratio of the bluff-body diameter (D_B) to the central fuel-jet diameter (D_J). Prade and Lenze [15] and Masri and Bilger [16] have provided measurements of mean composition in bluff-body stabilized flames using gas sampling probes. Some simultaneous single-point measurements of reactive and conserved scalars recently have been reported in these flames [17, 18]. Dally et al. [19] have reported on the evolution of nitric oxide, NO in bluff-body flames, and found that the structure of the recirculation zone and the fuel type affect its production. Schefer and Namazian [20, 21] have provided measurements of the

flow field as well as images of the reaction zones in various regions of bluff-body stabilized flames. A range of fuels with a range of D_B and D_J have been covered in the studies referenced here.

A number of numerical approaches are now potentially capable of simulating the structure of bluff-body stabilized flames. Classical methods based on Reynolds averaging and using the k-ϵ or Reynolds stress (RS) models of turbulence have a well-known discrepancy in predicting the correct spreading rate, decay rate, and length of the recirculation zone [18]. This problem recently has been overcome by adjusting one of the empirical constants in the dissipation transport equation [22, 23]. However, with these methods the problem of closure of the chemical source term remains unworkable. Other approaches are based on large eddy simulation (LES) [11, 24], flamelet models [9], conditional moment closure (CMC) [8], and probability density function (PDF) method [25, 26]. These, coupled with reduced chemical kinetics, are promising tools for simulating the structure of bluff-body flames.

In this paper, the mean compositional structure of bluff-body flames is first provided from single-point Raman/Rayleigh/LIF measurements. The root-mean-square (rms) fluctuations also are presented and the vortical structure in the recirculation zone is emphasized. This is followed by scatter plots of the instantaneous compositional structure and the joint conditional PDFs of various scalars. The instantaneous data are reported for the different regions in the jet, but the main focus is on the neck zone where the flames extinguish at high enough jet velocities. This region is ideal for the study of turbulence–chemistry interactions, and the data presented will reveal the extent of these interactions.

DATA COLLECTION AND REPORTING

Apparatus

The bluff-body burner has an outer diameter D_B = 50 mm with a concentric jet diameter D_J = 3.6 mm. The face of the bluff-body has a heat-resistant ceramic coating. The wind tunnel has an exit cross section of 254 × 254 mm. The coflow-air velocity is fixed at 40 m/s, and the free-stream turbulence level in the tunnel is ~2%. The single-point Raman/Rayleigh/LIF technique is used to measure temperature and the concentration of stable species, as well as the concentration of OH radical and NO. Data for NO are reported elsewhere [19] and only samples are presented here. The Rayleigh signal, which is proportional to the density of the sample at the probe volume, is used to determine the temperature by assuming ideal gas law. The Raman signals are used to determine the concentration of CO_2, CO, H_2O, H_2, O_2, N_2, and C—H (CH_4 or CH_3OH). Figure 1 shows a schematic illustration of the flame and the corresponding measurement locations. The distance of these locations from the exit plane of the burner is normalized by the bluff-body diameter D_B.

Figure 2 shows the optical arrangement for the single-point Raman/Rayleigh/LIF technique. The Raman/Rayleigh measurements use two Nd:YAG lasers where the successive pulses are stretched from ~8 to ~40 ns to avoid excessive energy in the probe volume and hence gas breakdown. The energy delivered to the probe volume is ~600 mJ. The combined Nd:YAG (532 nm) beams are reflected back through the probe volume using a collimating lens and a 180° turning prism, which effectively doubles the Raman and Rayleigh energy to ~1.2 J. These lasers give more consistent results than pumped-dye lasers, which suffer from line drift because of dye aging. The OH fluorescence measurements use a separate Nd:YAG-pumped-dye laser system. The OH excitation beam is tuned for the $O_{12}(8)$ transition in the $A^2\Sigma^+ - X^2\Pi$ (1, 0) band (λ = 287.9 nm), and the OH signal is collected through a broad-band colored glass filter, (Schott WG-295 and Hoya U-340, both 3 mm thick). This allows the capture of the fluorescence in both the (1, 0) and the (0, 0) bands. The NO excitation beam has a wavelength of 225.9 nm and the signal is collected from the system of bands at 236, 247, 259, and 271 nm.

The Raman and Rayleigh scattered light is collected using a six-element achromatic lens and is then collimated with a camera lens. The collimated Rayleigh light is reflected using a

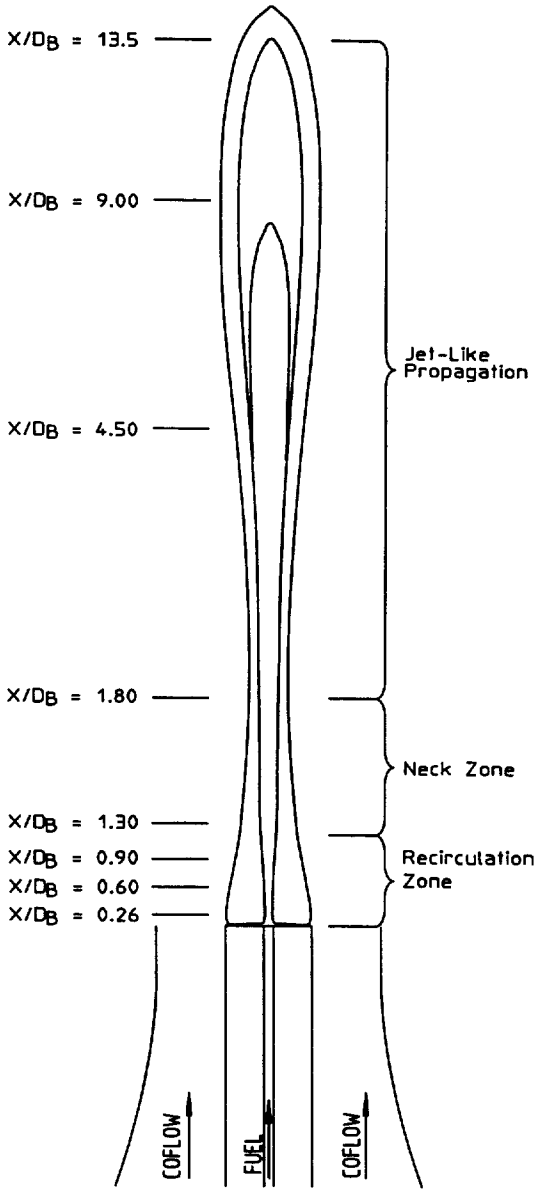

Fig. 1. Bluff-body stabilized flame and measurement locations.

holographic Raman edge filter and is focused onto a photomultiplier for detection, whereas the transmitted Raman collimated light is focused onto the entrance slit of a 0.75 m polychromator. This separation of the Rayleigh and Raman scattered light prevents the interference of the strong Rayleigh signal with the weak Raman signal. The OH and NO signals are collected using a Cassegrain mirror at the opposite side of the test section from the Raman/Rayleigh lens. Dichroic beam splitters are used to direct the different fluorescence signals onto the different detectors. For more details see Refs. 29 and 30.

Calibration of the Rayleigh system is based on measurements in nitrogen and helium at room temperature. Calibration of each channel of the Raman system is accomplished through measurements in room temperature gases and in an extensive series of flames established on a Hencken burner. This series includes H_2/air, CO/H_2/air, and CH_4/air flames operated over wide ranges in stoichiometry. Measurements are made at 30 mm above the burner, where the fuel/air mixture is fully burnt and homogeneous. Chemical equilibrium is assumed for these flames, and calibration factors at each temperature condition are determined using the equilibrium species concentrations. It is worth noting that this assumption may lead to systematic errors of 1–2% in some species at high temperatures because of radiation loss from the flames, even though the burner itself is nearly adiabatic. To improve the calibration of the Raman species in the intermediate temperature range, the calibration gases are heated up electrically to ~900 K, and Raman/Rayleigh measurements are taken at roughly 100 K intervals, providing calibration data between ambient and lean flame temperatures. Polynomial curve fits in temperature are generated for the response of each of the Raman channels. The cross talk between the Raman species also is measured in these calibration flows and flames, and correction curves as functions of temperature are deduced.

The OH calibration is based on measurements above a premixed CH_4/air flat flame where the OH concentration has been determined by laser absorption. The NO calibration uses a lean premixed $CH_4/O_2/N_2$ flame stabilized on a water cooled McKenna burner. Portions of the N_2 flow are progressively replaced by N_2 doped with 200 ppm of NO, which is known to survive passage through this flame. The quantitative OH and NO concentrations in the turbulent flames are obtained by correcting the fluorescence signals on a shot-to-shot basis for the variations in the Boltzmann fraction and the collisional quenching rate, which are determined from the measured temperature and

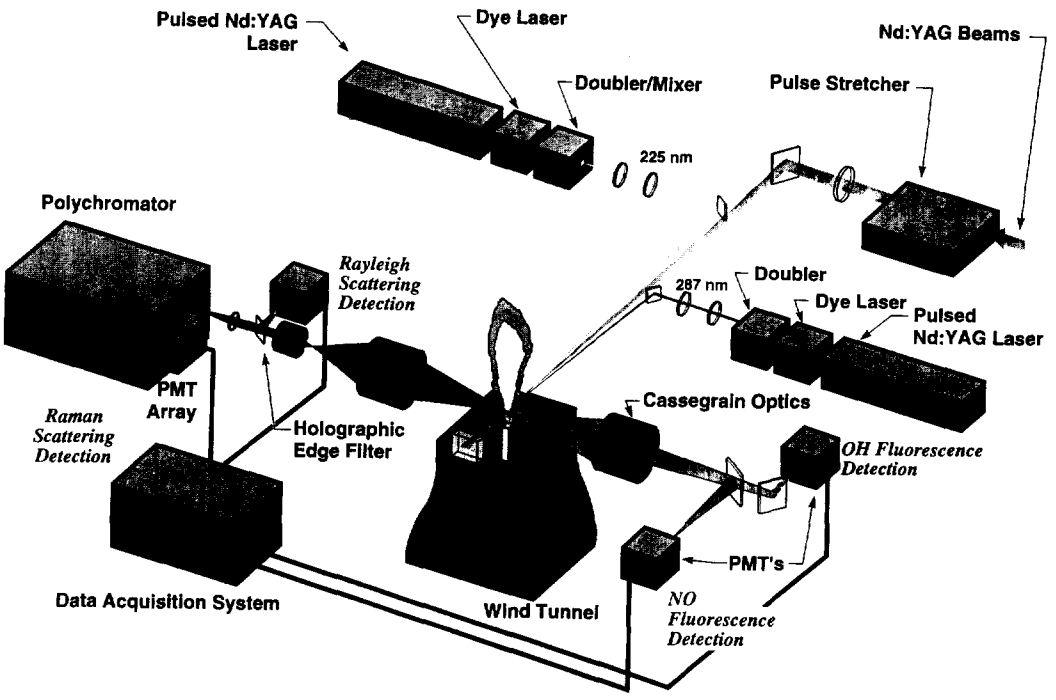

Fig. 2. Arrangement for the single-point Raman/Rayleigh/LIF technique.

species concentrations. Calibrations are performed at the beginning and end of each day of data collection.

Three different fuels are investigated: CH_3OH, H_2/CO (2:1), and H_2/CH_4 (1:1) by volume. The first two fuels have a stoichiometric mixture fraction of 0.135, whereas the third has a stoichiometric mixture fraction of 0.050. Methanol is evaporated and delivered through a heated line before being released at 100°C from the jet. Methanol fuel is used because its chemistry is intermediate in complexity between H_2/CO and CH_4 fuels. A list of the flames investigated and some relevant parameters are given in Table 1.

The fuel-jet velocity is varied to investigate the Damköhler number effects on gas emissions, localized extinction (LE) in the neck zone, and the structure of the recirculation zone. All flames have soot-free recirculation zones. The measurements are made at different axial locations in the flame starting at X/D_B = 0.26, which is closest to the burner. This location is representative of the core of the outer vortex where the mixture is almost uniform in all flames. Typically, 800 shots are collected at

TABLE 1

Flames Studied and their Parameters

Fuel	Flame	U_J/U_{CO}	Re_J	% BO	$T_{IN}(K)$	ξ_s	$\dot{M}_J(N)$	$T_{ad}(K)$
CH_3OH	ML1	80/40	23,700	55	373	0.135	43.70E-3	2260
	ML2	121/40	35,900	84			99.90E-3	
	ML3	134/40	39,700	93			122.60E-3	
H_2/CO (2:1)	HC1	134/40	17,500	18	298	0.135	50.90E-3	2400
	HC2	321/40	41,990	43			292.1E-3	
	HC3	536/40	70,120	74			814.6E-3	
H_2/CH_4 (1:1)	HM1	118/40	15,800	50	298	0.05	33.70E-3	2265
	HM2	178/40	23,900	75			76.80E-3	
	HM3	214/40	28,700	91			111.1E-3	

each radial location covering the entire width of the flame. Measurements in flames ML3 and HC3 are restricted to the neck zone and only the instantaneous data are presented for these flames.

The mixture fraction for each data point was calculated using Bilger's [31] formula:

$$\xi = \frac{\frac{2(Z_C - Z_{C,O})}{W_C} + \frac{(Z_H - Z_{H,O})}{2W_H} - \frac{2(Z_O - Z_{O,O})}{W_O}}{\frac{2(Z_{C,F} - Z_{C,O})}{W_C} + \frac{(Z_{H,F} - Z_{H,O})}{2W_H} - \frac{2(Z_{O,F} - Z_{O,O})}{W_O}} \quad (1)$$

where Z_i is a conserved scalar given by the total mass fraction of element i, and W_i is the atomic mass of element i. This formula preserves the stoichiometric value of the mixture fraction and accounts for the effect of the differential diffusion. It should be noted here that if differential diffusion effects are nonexistent, the mixture fraction calculated from Eq. 1 will then be identical with that computed separately from each of the atomic balances.

Measurements Uncertainty

Three types of errors are associated with the measurements: random, systematic, and interference error. Random error includes shot and electronic noise and determines the precision of the single-point data. The measurement precision may be obtained for each species by measuring in a uniform medium of fixed concentration.

Sources of systematic error include calibration error, as well as error associated with the optics. The drift in the calibration factors and errors associated with measuring laser energies contribute to systematic error and hence to uncertainty.

The third type of error is caused by interference from a range of sources including nonresonant fluorescence, incandescence, and luminescence, as well as Raman interference on other species. Interference error varies significantly with fuel type as well as stoichiometry. The sources of interferences are very difficult to quantify and are not considered further in this section. Errors due to spatial resolution are considered separately in the next section. A detailed discussion of error sources in typical combustion laser diagnostics is given by Eckbreth [32].

The accuracy of single-point data is determined by a combination of random, systematic and interference error. The contribution of random error to the averaged data is less significant and depends on its correlation with the systematic error. Quantifying the accuracy of the averaged data is very difficult and is not attempted here. However, estimates are presented on the precision of the single-point data.

Figure 3 shows signal-to-noise ratios obtained from the calibration data of the Rayleigh signal, a range of Raman signals and the OH LIF signal. The Rayleigh signal-to-noise ratio ranges from ~150 at temperatures of ~2500 K to ~400 at room temperature. The signal-to-noise ratio for the Raman species and OH increases with number density and ranges from ~10 to ~60, depending on the species. For N_2, which is not shown here, the signal-to-noise ratio ranges from ~65 to ~125. Signal-to-noise ratios presented here include both random and systematic error but do not account for interferences and spatial resolution error. Table 2 shows estimates of the precision of single-point measurements of various species concentrations for two typical samples collected in a methane/hydrogen flame. Lean and rich sample compositions are obtained from the actual data and are taken here as illustrations of typical measurement conditions. The percentage error increases with decreasing number density, or mole fraction, as shown in Fig. 3. At a mole fraction of ~5% the error is ~5% on CO_2 and 8% on CO, increasing to 9% when the mole fraction is ~2%. Water at a mole fraction of ~12% has an associated error of ~4%. The uncertainty on the NO measurements was reported by Barlow and Carter [33], and the maximum estimated error was ~10%.

The overall error should, of course, include fluorescence interference and spatial resolution effects, which are difficult to quantify. The

TABLE 2

Sample Estimates of Error Associated with Measured Species Concentrations for Two Typical Sample Compositions

Sample	Temperature	Species	% Mass Fraction	Number Density	% Error
Lean	1900	O_2	4.0	0.12×10^{18}	10.0
		N_2	75.0	2.63×10^{18}	0.8
		CO_2	8.0	0.18×10^{18}	4.5
		CO	2.0	0.07×10^{18}	9.0
		H_2	0.5	0.23×10^{18}	12.5
		H_2O	11.0	0.60×10^{18}	5.0
		OH	0.3	0.02×10^{18}	3.8
Rich	1400	CH4	18.0	1.09×10^{18}	2.3
		N_2	57.0	1.98×10^{18}	1.1
		CO_2	5.5	0.12×10^{18}	5.5
		CO	5.5	0.19×10^{18}	8.3
		H_2	2.5	1.22×10^{18}	4.0
		H_2O	12.0	0.65×10^{18}	4.0

fluorescence interference peaks on the rich side of stoichiometric and affects the Raman signals in ranging degrees. It is estimated that errors associated with the fluorescence interference are generally less than 10%.

Spatial Resolution

Spatial resolution effects on the various scalars measured in turbulent flames by the Raman/Rayleigh/LIF technique have been studied by Mansour et al. [34], who gave an estimate of those effects on the measured variance of the scalar quantities in terms of l_p/L_θ, Re_t and l_p/L_u. The turbulence Reynolds number is defined as $\mathrm{Re}_t = u'L_u/\nu$. For the experiment reported here, $l_p = 0.8$ mm and $L_u = 10$ mm in the inner region (taken as the width of the inner vortex) and 15 mm in the outer region (taken as the width of the outer vortex close to the burner). At $X/D_B = 0.26$ and $r/R_B = 0.06$ $L_\theta = 80$ mm and Re_t peaks at 12,200, while at the core of the outer vortex ($r/R_B \geq 0.25$) where $L_\theta = 9$ mm and Re_t is 830. The rms fluctuations of the velocity u' have not been measured and are taken from the calculated velocity field of the same flames and conditions using the RS model for turbulence and the "mixed is burnt" combustion model.

From a chart introduced by Mansour et al. [34] the estimated error due to spatial resolution is determined as the ratio of the variance of the scalar θ that would be measured given the

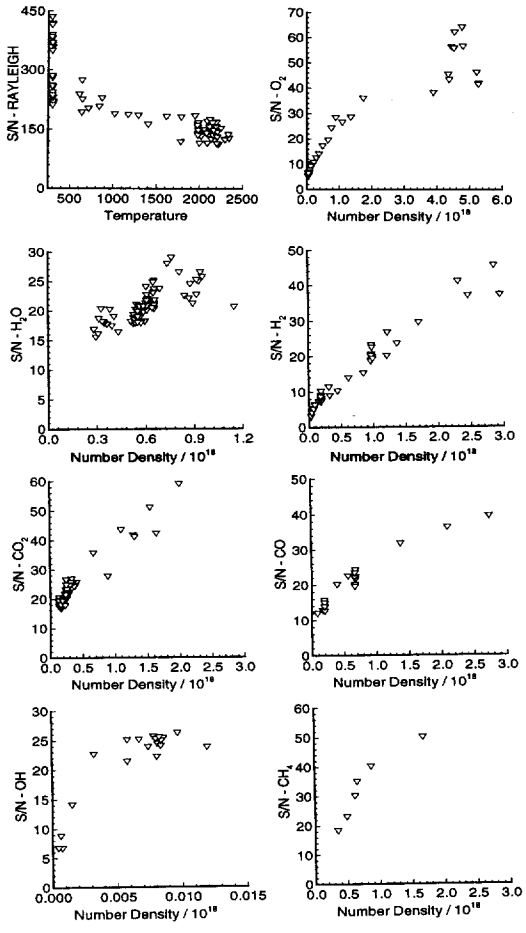

Fig. 3. Signal-to-noise ratio for Rayleigh, Raman, and OH LIF signals vs temperature for Rayleigh and vs number densities for the measured species.

probe dimensions and the flow field details and the actual variance of the same scalar θ, $(\langle \overline{\theta'^2}_m / \overline{\theta'^2} \rangle)$. In these bluff-body flames the maximum spatial resolution error estimated from the chart is 9% at $X/D_B = 0.26$ and $r/R_B = 0.06$. At all locations where $r/R_B \geq 0.25$ the error is less than 4%. These are acceptable levels knowing that the probe volume is about five times larger than the smallest Kolmogorov length scales at the measurement locations.

Laminar Flame Calculations

The structures of steady laminar diffusion flames are computed for each mixture over a range of stretch rates from detailed chemical kinetics. The computed results are shown on the scatter plots and serve as guides for the data rather than absolute limits. They also are used to determine the reactedness of each data sample. Laminar flame calculations normally account for differences in species diffusivities and hence for a nonunity Lewis number Le $\neq$ 1.0. In turbulent flames, the effects of differential diffusion depend on the original fuel mixture but are expected to decrease with $(\mathrm{Re}^{-1/2})$ [35]. Although mixtures of fuels with widely different diffusivities, such as H_2, CO, and CO_2, are expected to yield significant differential diffusion effects, results for such flames show this not to be the case even at modest jet Reynolds numbers [36].

The mixture fractions calculated for the experimental data using different conserved scalars, such as C and H atoms, are in good agreement with those calculated from Eq. 1, implying that there is little or no differential diffusion effects. It may, therefore, be more realistic to compare turbulent flame composition with those computed for laminar flames where Le = 1.0 and the differential diffusion effects are suppressed. Computations are shown in Fig. 4 for the steady laminar diffusion flames of the H_2/CO (left column) and CH_3OH (right column) fuels, with and without equal mass diffusivities. The computed temperature and percentage mass fraction of CO, CO_2, H_2, H_2O, OH, and H are plotted vs the mixture fraction at a moderate stretch rate $a = 100\ \mathrm{s}^{-1}$. The dotted lines are for the equal diffusivity case, with Le = 1.0 and equal species mass diffusivities, whereas the solid lines are for variable diffusivities. The square symbols are for species scaled with the left vertical axis whereas the triangular symbols are for species scaled with the right axis. It can be seen from this figure that differential diffusion has substantial effects on the magnitude and trend of stable species as well as transient flame radicals. In the H_2/CO flame the peak mass fraction of CO_2 increases from ~5 to 12.5% when equal diffusivities are assumed. Moreover, the location of the peak shifts from $\xi = 0.35$ and overlaps with the location of temperature and water peaks at $\xi = 0.135$. The methanol flame also shows differences in the computed structure with the peak mass fraction of H_2 almost doubling for the equal diffusivity case. The peak mass fraction of radicals like H and OH are affected in different proportions, depending on the stretch rate and the fuel mixture. The effects of differential diffusion on the H_2/CH_4 flame are also significant for all species (the computations are not presented here). These results are consistent for other stretch rates.

The laminar flame compositions used in the rest of this paper are calculated with Le = 1.0 and equal species mass diffusivities.

Conditional PDFs

The reactedness of a fluid parcel can be calculated for any of the reactive scalars as follows:

$$b_i = \frac{P_i - P_F}{P_L - P_F} \tag{2}$$

where b_i is the reactedness of scalar i, P_i is the measured scalar, and P_L and P_F are the "fully burnt" and "frozen" values of the scalar i at the measured mixture fraction, respectively. The fully burnt scalar values are taken from the laminar diffusion flame calculations for the fuel mixture at low stretch rate ($a = 5\ \mathrm{s}^{-1}$), whereas the frozen values are calculated for the isothermal case at room temperature. The reactedness ranges between 0, which denotes an unreacted sample, and 1.0, which denotes fully burning sample.

The PDF of the reactedness conditioned with respect to the mixture fraction is a good measure of the extent the reaction progress for each scalar. The conditional probability density func-

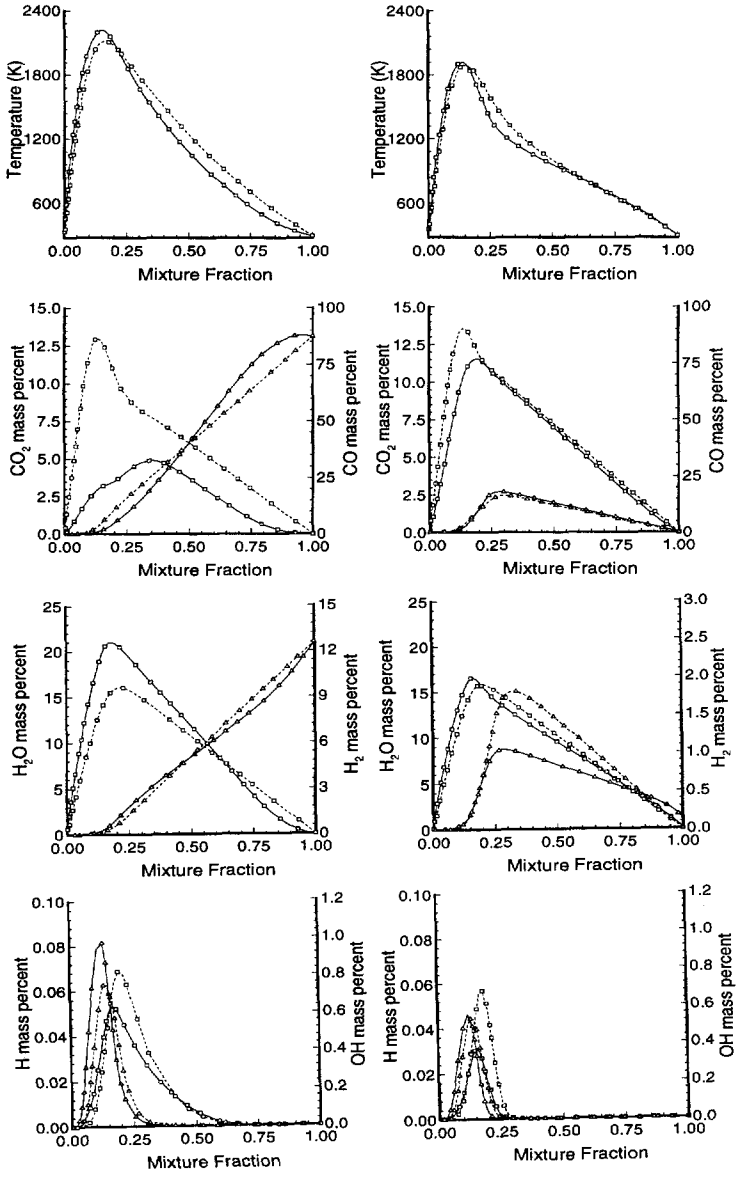

Fig. 4. Temperature and species percentage mass fractions computed for the steady laminar diffusion flame with differential diffusion (solid lines) and without differential diffusion (dashed lines) plotted against the mixture fraction for the H_2/CO(2/1 by Vol.) fuel (left column) and for the CH_3OH fuel (right column); stretch rate $a = 100\ s^{-1}$. Left axis is for lines with square symbols while right axis is for lines with triangle symbols.

tions (CPDFs) are calculated for a reactedness range of -0.1 to 1.1 to allow for any experimental errors in the single-point data. This range is divided into a number of intervals and the data in each mixture fraction range is allocated to each interval according to the value of the reactedness b. The probability of b being in the interval bounded by x and y is calculated as follows:

$$p(x < b < y) = \frac{1}{\Delta b_{x,y}} \frac{n_{b,x,y}}{N} \tag{3}$$

where $n_{b,x,y}$ is the number of samples with the scalar b between x and y, N is the total number of data points considered, and $\Delta b_{x,y}$ is the width of the interval bounded between x and y.

The CPDFs of the reactedness have been calculated for a range of reactive scalars. For each scalar the CPDFs of the reactedness for three mixture fraction intervals are calculated. These intervals are *lean*, $0.4 \le \xi/\xi_s < 0.8$; *stoichiometric*, $0.8 \le \xi/\xi_s < 1.2$; and *rich*, $1.2 \le \xi/\xi_s < 1.6$.

RESULTS

The jet dominant bluff-body stabilized flames are characterized by three distinct zones, shown schematically in Fig. 1. The recirculation zone extends about one bluff-body diameter downstream of the face of the burner. It has an outer larger vortex close to the air side and, depending on the flow, an inner vortex adjacent to the central jet [23]. Generally, the outer vortex has a nearly uniform mixture fraction close to the face of the burner and its mixture strength ($\bar{\xi}_{vo}/\xi_s$) depends on the fuel and flow conditions. Here, $\bar{\xi}_{vo}$ is the mean mixture fraction in the outer vortex and ξ_s is the stoichiometric mixture fraction. The inner vortex, which is close to the fuel jet and the turbulent shear layer, is narrower and has a rich nonuniform mixture. When increasing the jet momentum flux relative to the coflow, the jet expands and shifts the core of the inner vortex downstream until it loses its circulating pattern and becomes part of the jet. At the same time the outer vortex becomes shorter and smaller. Chen et al. [37] have reported a similar behavior in swirl stabilized flames and suggested nondimensional parameters based on the jet momentum flux to quantify the strength of the circulating vortices.

Downstream of the recirculation zone is a region of intense mixing where local extinction and blow-off occur when the jet velocity is sufficiently high. This is referred to as the neck zone and is an ideal region of the flame for studying more extreme effects of turbulence–chemistry interaction. The third region is the rest of the flame, which spreads in a jet-like manner. At a sufficiently high jet velocity, this region shows some reignition characteristics, similar to those found in the piloted stabilized flames.

Mean Compositional Structure

Radial profiles of the Reynolds averaged and rms fluctuations of measured reactive scalars mass fractions are presented here for each fuel separately and for a range of jet velocities. Only selected data deemed necessary to reveal the mixing and composition pattern of these flames are shown. The remaining data may be accessed on the worldwide web [1].

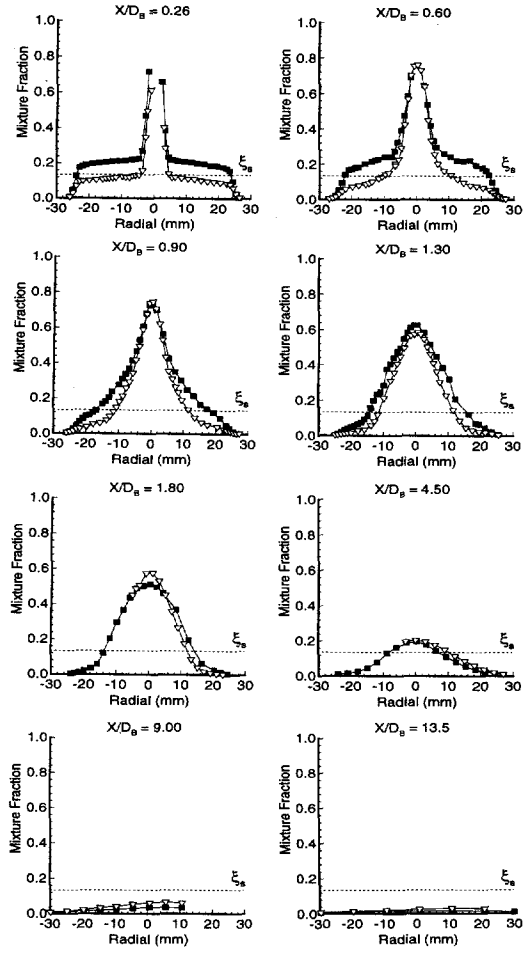

Fig. 5. Radial profiles of mean mixture fractions plotted for different axial locations along full length of methanol flames. Black squares, for ML1 flame; triangles, for ML2 flame; and dashed line, for stoichiometric value.

CH_3OH Flames

Two flames of methanol fuel are reported. The first flame (ML1) has a fuel-jet velocity of 80 m/s; the second flame (ML2) has a jet velocity of 121 m/s. These correspond to 55 and 84% of the blow-off velocity, respectively. Visibly, flame ML1 exhibits a luminous outer vortex extending to approximately one bluff-body diameter. Flame ML2 on the other hand, does not show any visible outer vortex and its recirculation zone is slightly shorter.

Radial profiles of mean mixture fraction plotted at different axial locations along the full length of both flames ML1 and ML2 are shown in Fig. 5. At axial location $X/D_B = 0.26$ in both

flames, the outer region has a relatively flat profile of the mean mixture fraction $\bar{\xi}$. In flame ML1, the outer vortex is slightly rich with $\bar{\xi} = 0.2$, whereas in flame ML2 the mean mixture fraction in the same region is $\bar{\xi} = 0.125$, which is slightly lean of the stoichiometric value. This is why the outer vortex of flame ML2 is nonluminous. Further downstream, but still inside the recirculation zone ($X/D_B < 1.3$), the mean mixture fraction profiles in the two flames are less uniform and have comparable values at the centerline. In the neck zone and for the rest of the flame, the profiles have similar trends in both flames. At locations downstream of the neck zone ($X/D_B > 1.8$) the ML2 flame has a higher mean mixture fraction than flame ML1 at all radial locations.

In Fig. 6, the rms fluctuations of the mixture fraction, $(\overline{\xi'^2})^{1/2} \equiv \xi'$, across both flames are plotted for the same axial locations as in Fig. 5. These profiles are very useful in identifying mixing patterns by regions of high values of ξ'. Three distinct mixing layers are observed in the recirculation zone. The first lies in the outer edge of the outer vortex where mixing between this vortex and the coflowing air occurs. This is indicated by the slight increase in the rms fluctuation at this region. The second layer of mixing lies between the inner and outer region and is identified by a gradual increase in the rms fluctuations of the mixture fraction especially at locations $X/D_B = 0.6$ and 0.9. The third mixing layer is characterized by a sharp increase in ξ' close to the jet axis and is located in the region between the inner vortex and the fuel jet. Note that at $X/D_B = 0.26$, the intermediate mixing layer is lost because the lower part of both inner and outer vortices are already well mixed and have uniform composition.

Figure 7 shows radial profiles of mean temperature $\bar{T}$ plotted for the same axial locations as in Figs. 5 and 6 for flames ML1 and ML2. Figure 8 shows radial profiles of mean and rms fluctuations of mass fraction of the hydroxyl radical ($\bar{Y}_{OH}$ and Y'_{OH}) plotted for axial locations $X/D_B \leq 1.3$ for flames ML1 and ML2. It is apparent that in flame ML1 the peak mean temperature occurs at the air-side edge of the outer vortex and this is consistent with a sharp peak in the OH concentration. For flame ML2, peak $\bar{T}$ and $\bar{Y}_{OH}$ occur at $r/R_B = 0.36$ (where

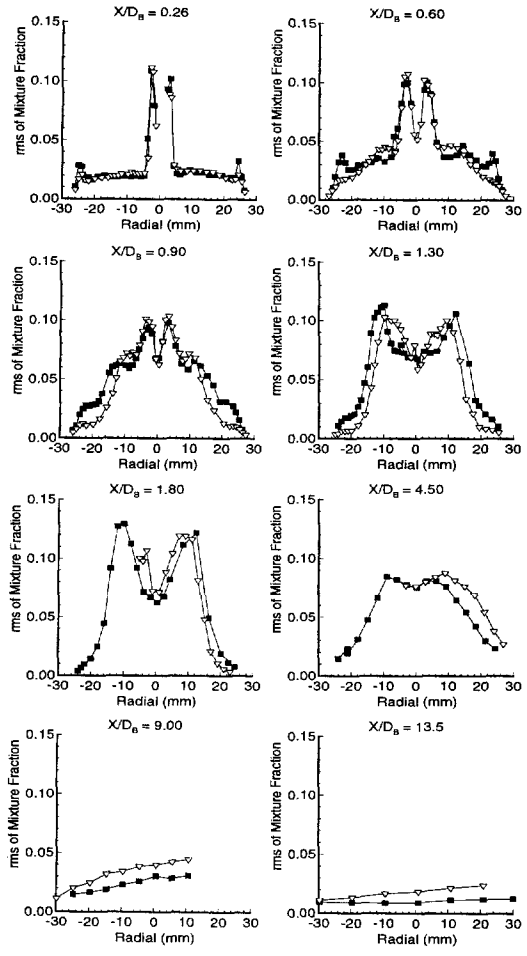

Fig. 6. Radial profiles of rms fluctuations of mixture fraction for different axial locations along full length of methanol flames. Black squares, for ML1 flame; triangles, for ML2 flame.

R_B is the bluff-body radius), which is at the edge of the inner vortex. This confirms that for flame ML1, the reactive zone occurs at the outer edge of the outer vortex, whereas in flame ML2 it is closer to the inner vortex inside the recirculation zone. This observation is consistent with the disappearance of the visible flame in the outer vortex of flame ML2. The highest peak mean temperature of 1900 K is found at the axial location $X/D_B = 0.26$ in both flames and it drops to around 1500 K at the neck zone. Previous observation in such flows [16] reported the same temperature depression in the neck zone due to intense mixing.

At axial locations $X/D_B = 0.26$, 0.6, and 0.9

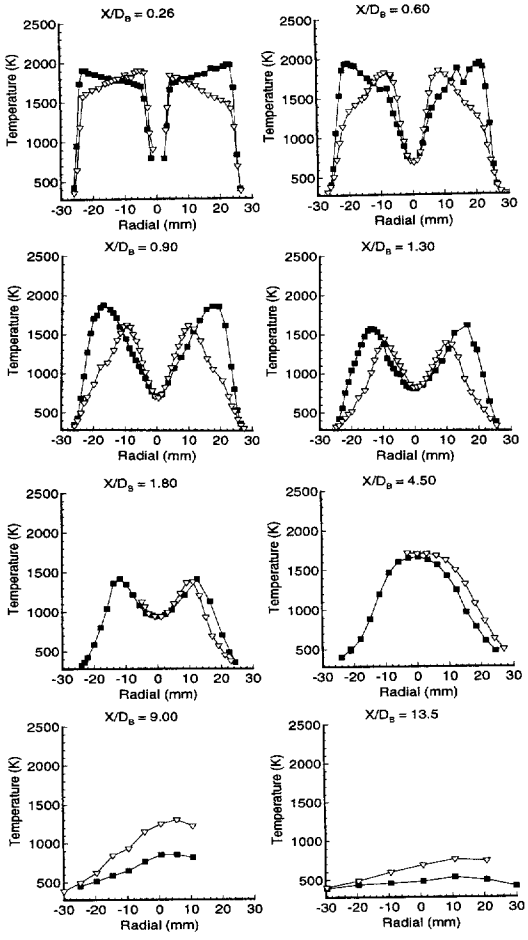

Fig. 7. Radial profiles of mean temperatures for different axial locations along full length of methanol flames. Black squares, for ML1 flame; triangles, for ML2 flame.

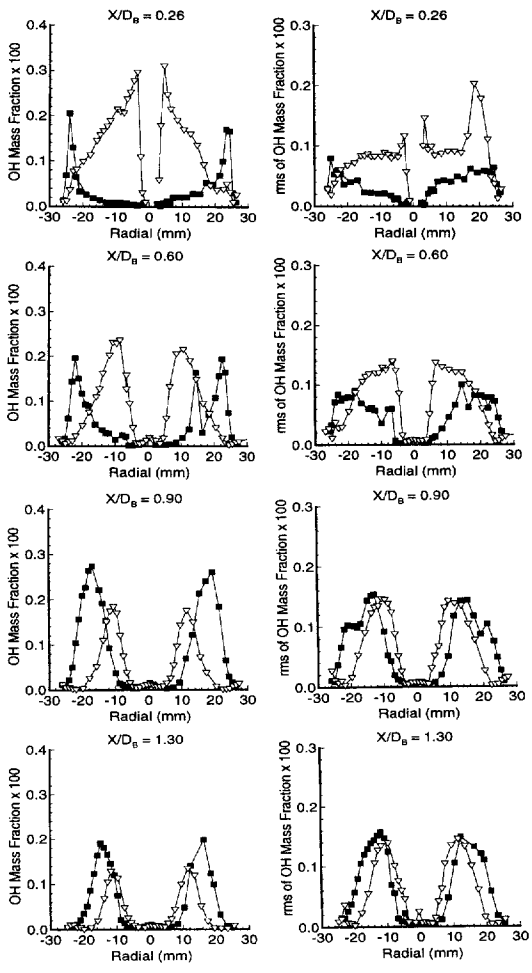

Fig. 8. Radial profiles of mean and rms fluctuations of the OH mass fractions for different axial locations in the methanol flames. Black squares, for ML1 flame; triangles, for ML2 flame.

the peak OH in flame ML1 occurs on the air side of the outer vortex, whereas for flame ML2 the peak OH is very close to the fuel jet. The very narrow profile of OH in flame ML1 is consistent with the mean mixture in this flame, which is generally rich in the outer vortex and becomes stoichiometric only on its outer (air side) edge. Downstream of the recirculation zone the peak in the OH profiles of both flame ML1 and flame ML2 overlap and are generally lower than those attained in the recirculation zone. At $X/D_B = 1.3$, still inside the intense mixing neck, peak values of OH radical in flame ML2 are lower than those in flame ML1. This is caused by the higher mixing rate and finite-rate chemical kinetics effects, which lead to samples extinguished locally, as discussed later. Further downstream (not shown here) at $X/D_B > 4.5$ peak values of OH in both ML1 and ML2 flames are close but are still much lower than those attained further upstream.

The rms fluctuation of the OH mass fraction Y'_{OH} profiles show wider distribution in flame ML2, which is consistent with the mean hydroxyl profiles. At $X/D_B = 0.9$, the peaks in Y'_{OH} occur at $r/R_B \approx 0.4$ and 0.56, which coincide with the intermediate mixing layer and the rich side of the reaction zone, respectively. Also, the peak of Y'_{OH} is of the same order as the peak of $\bar{Y}_{OH}$ right across the flame. It should be noted here, that the high value of Y'_{OH} is not

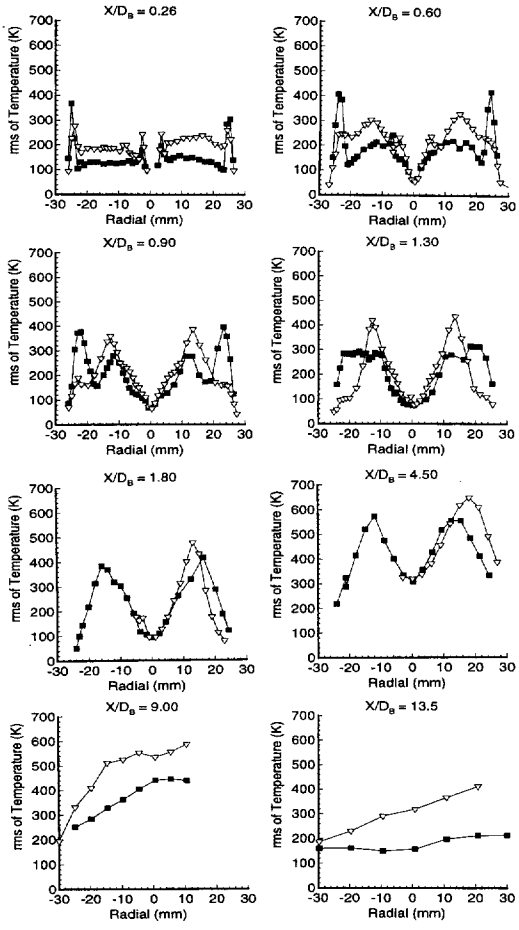

Fig. 9. Radial profiles of rms fluctuations of the temperature plotted for different axial locations along full length of methanol flames. Black squares, for ML1 flame; triangles, for ML2 flame.

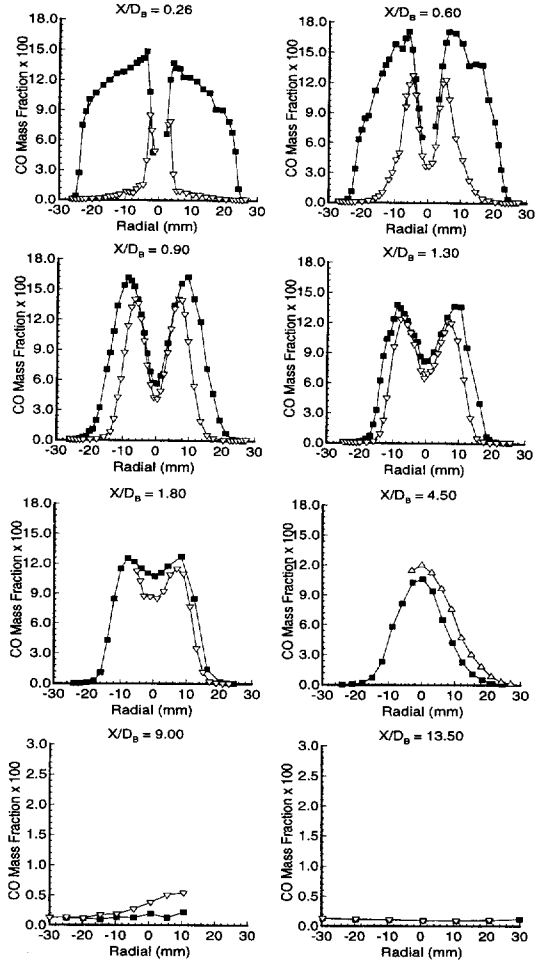

Fig. 10. Radial profiles of mean CO mass fractions for different axial locations along full length of methanol flames. Black squares, for ML1 flame; triangles, for ML2 flame.

caused by local extinction causing fluctuations in the OH signal. Scatter plots of Y_{OH} vs ξ (shown later) plotted for the reaction zone of both flames ML1 and ML2 indicate that fluid samples are burnt fully and there is no sign of significant local extinction at this downstream location. The rms fluctuations plotted vs the radial distance are therefore caused by turbulent fluctuations in the mixture at the given radial location.

Figure 9 shows radial profiles of rms fluctuations of the temperature T' plotted for the same axial locations as in Figs. 5–7. Within the recirculation zone, an increase in the rms fluctuations of the temperature is detected at the same radial locations where local maxima in ξ' occur. At $X/D_B = 0.9$, which is near the tip of the recirculation zone, flames ML1 and ML2 show double maxima in the rms fluctuations of temperature at $r/R_B \approx 0.4$ and 0.88, corresponding to the intermediate and outer mixing regions. A third peak in the rms of temperature is detected in the inner mixing region for flame ML2, because in this flame burning occurs in the inner zone where the temperature gradients are steeper. The profiles of Y'_{OH} shown earlier have a different pattern to that of T', due to the fact that OH profiles are narrower and decrease to zero closer to the jet centerline.

Figure 10 shows radial profiles of the mean

mass fraction of CO, plotted for axial locations along the full length of the flames. Profiles for the H_2 mean mass fractions (not shown here) show very similar trends to those of CO plotted in Fig. 10. These two species (CO and H_2) are produced by the pyrolysis of rich methanol mixtures and burn to CO_2 and H_2O at the stoichiometric mixture fraction. The early appearance of CO and H_2 also was observed by Masri et al. [27] in pilot-stabilized diffusion flames. Mean mass fractions of CO close to the tip of the recirculation zone are slightly higher in flame ML1 than in flame ML2. While at upstream locations, $X/D_B = 0.26$ and 0.6, the CO levels are much higher in flame ML1 than ML2. The difference in the CO levels results from the difference in the mixing fields for each flame. In flame ML1, this species is formed in the outer vortex of the recirculation zone where the mean mixture is rich, whereas in flame ML2 the species are formed in the inner vortex where conditions are also favorable. At downstream locations ($X/D_B = 4.5$), marginally higher concentrations of CO are found in the ML2 flame compared with the ML1 flame.

Figures 11 and 12 show radial distributions of mean and rms fluctuations of the CO_2 mass fraction, respectively, plotted for various axial locations. From these figures it is obvious that the shift in the stoichiometric contour within the recirculation zone from the inner vortex to the outer one has minor effect on the concentrations of CO_2. At locations inside the recirculation zone ($X/D_B < 1.3$) comparable levels of this species can be found for both flames and, not surprisingly, the shape of the profiles follow that of the temperature in each flame. Further downstream of the recirculation zone ($X/D_B = 1.8$) flame ML1 has CO_2 concentration profiles similar to those in flame ML2, whereas at higher axial locations $X/D_B > 4.5$, the CO_2 levels are significantly higher in flame ML2 than with flame ML1. The higher levels of CO_2 in flame ML2 are consistent with the higher mean mixture fraction measured for flame ML2 at these locations, as shown earlier in Fig. 5.

The rms fluctuations of CO_2 show similar features to the rms fluctuation of temperature shown in Fig. 9. In the recirculation zone, the Y'_{CO_2} peak in the mixing regions corresponds to the inner, intermediate, and outer zones. Further downstream at $X/D_B = 1.8$ and 4.5, Y'_{CO_2} shows a single peak at the radial location $r/R_B = 0.6$, which corresponds to the lean side of stoichiometric. For other products such as H_2O (not shown here) the mean and rms fluctuations exhibit similar patterns to those for CO_2. At locations $X/D_B = 9.0$ and 13.5 there is a slight asymmetry in the scalar profiles due to the difficulty in determining the centerline at these downstream locations.

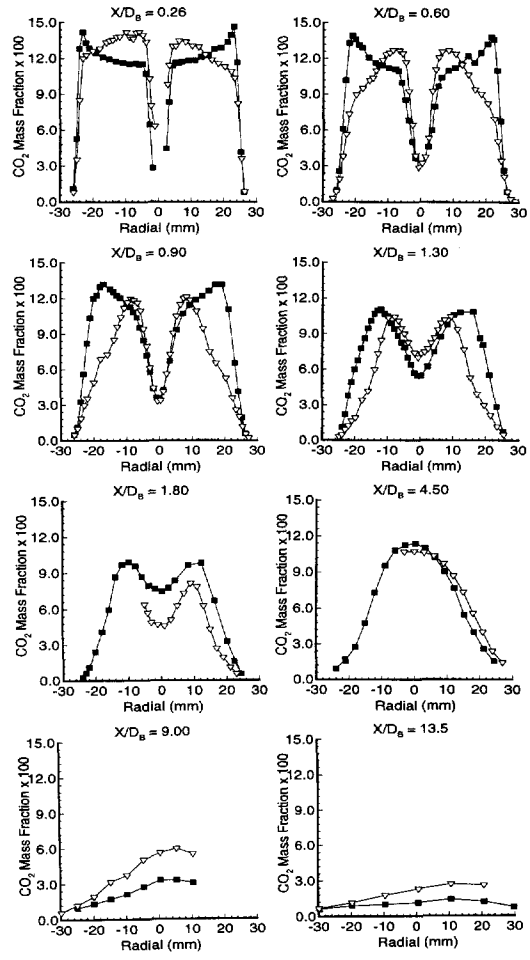

Fig. 11. Radial profiles of mean CO_2 mass fractions for different axial locations along full length of methanol flames. Black squares, for ML1 flame; triangles, for ML2 flame.

H_2/CO Flames

This fuel mixture has the same stoichiometric mixture fraction ($\xi_s = 0.135$) as methanol and

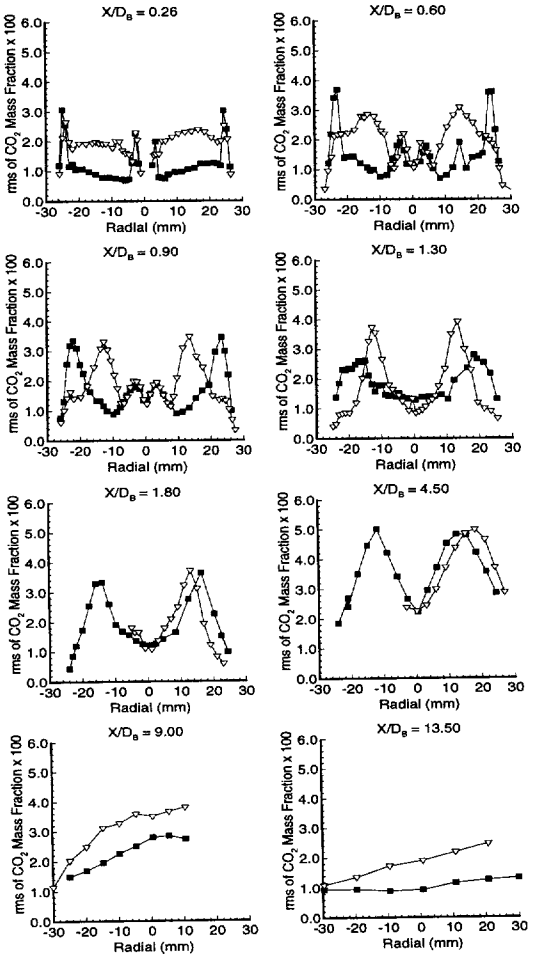

Fig. 12. Radial profiles of rms fluctuation of the CO_2 mass fraction for different axial locations along full length of methanol flames. Black squares, for ML1 flame; triangles, for ML2 flame.

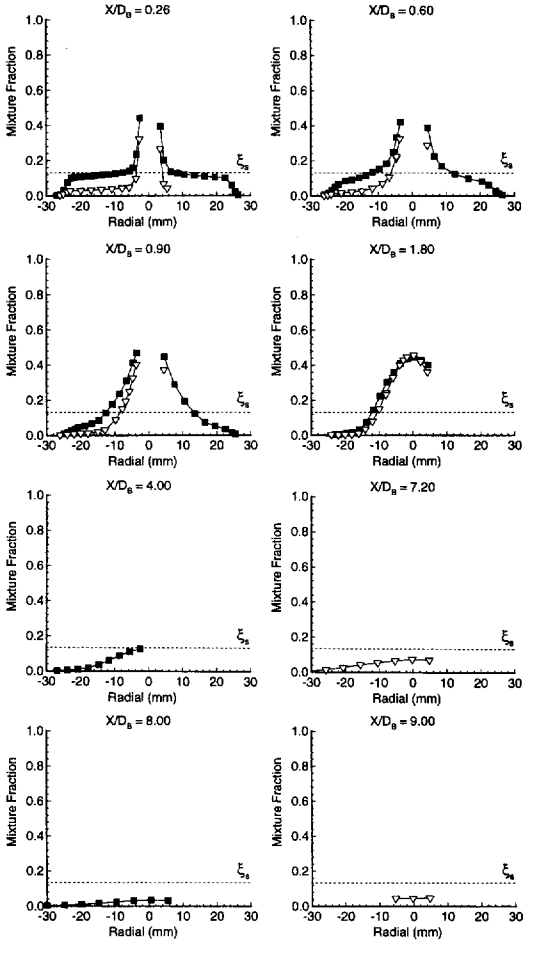

Fig. 13. Radial profiles of mean mixture fractions for different axial locations along full length of H_2/CO flames. Black squares, for HC1 flame; triangles, for HC2 flame; and dashed line, for stoichiometric value.

has the same ratios of elemental C, H, and O. Numerical studies of laminar diffusion flames of methanol show that the parent fuel decomposes to CO and H_2 on the rich side of stoichiometric and these burn out to CO_2 and H_2O at stoichiometric mixture fraction. The early appearance of CO and H_2 also was observed by Masri et al. [27] in the pilot-stabilized diffusion flames. This study will illustrate that significant differences exist between the H_2/CO and the CH_3OH flames despite the similarity in the atomic composition.

For this fuel mixture, the velocity at extinction was not determined experimentally because of limitations of the experimental rig. However, a velocity of 697 m/s was achieved for a flame that visually appears to be very unstable. This velocity is estimated to be ~95% of the velocity at extinction. Measurements are presented for two flames, the first with a fuel-jet velocity of 134 m/s (HC1), the second with one of 321 m/s (HC2). These velocities correspond to ~18 and ~43% of the velocity at extinction, respectively. The high velocity flame HC2 has no visible outer vortex and its recirculation zone extends to ~1.2 bluff-body diameters, whereas the low velocity flame HC1 has a visible, shorter outer vortex that extends to $X/D_B = 0.8$. Both flames have a similar visible length of $X/D_B \approx 9.0$.

Figure 13 shows the radial profiles of mean

mixture fraction, plotted for different axial locations along the full length of both flames. It is apparent that the outer vortices of the H_2/CO flames have similar characteristics to those observed in methanol flames. The core of these vortices, at an axial location $X/D_B = 0.26$, have a uniform mean mixture fraction that is slightly rich in flame HC1 with $\bar{\xi} = 0.15$. The mixture at this location in the recirculation zone becomes leaner with increasing jet velocity in the HC2 flame with $\bar{\xi} = 0.05$. The burning patterns, however, are different in flames HC1 and HC2 compared with those of flames ML1 and ML2, respectively. Flame HC1 has a slightly rich mixture on average in the core of its outer vortex, resulting in a wider reactive zone. The mixture in flame ML1 is richer and the reactive zone is thinner and closer to the outer edge of the outer vortex. Flame HC2, on the other hand, is much leaner than that of flame ML2 and this also results in a thinner reactive zone in this flame compared with the ML2 flame, where the reaction zone is closer to the inner region.

In Fig. 14 the radial profiles of the rms fluctuations of mixture fraction are plotted for the same axial locations as in Fig. 13. The rms profiles of mixture fraction for these flames are similar to those of methanol flames. Three distinct mixing layers are present in the recirculation zone, as observed for the methanol flames. The inner layer at the interface between the fuel jet and the inner vortex, the intermediate layer between the inner and outer vortices, and the outer layer between the coflow air and the outer vortex.

The radial profiles of mean and rms fluctuations of the temperature, shown in Fig. 15, exhibit a distinct trend in each one of the H_2/CO flames. A difference of up to ~800 K in the peak mean temperature can be seen at location $X/D_B = 0.26$ for the two flames. The temperature drop in flame HC2 is consistent with the lean mixture found at this location in the flame. Here, the hot products that are formed in the inner region mix with cold air from the coflow and produce a relatively cold mixture in the outer vortex. For the rest of the recirculation zone the difference in the temperature profiles in both flames decreases gradually and an almost identical distribution can be found at location $X/D_B = 1.8$ in the neck zone. Further

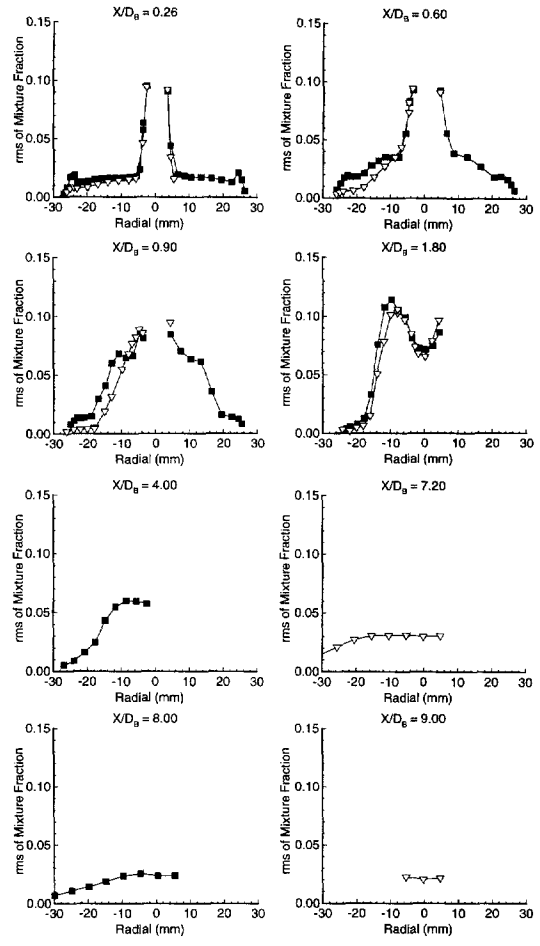

Fig. 14. Radial profiles of rms fluctuations of the mixture fraction for different axial locations along full length of H_2/CO flames. Black squares, for HC1 flame; triangles, for HC2 flame.

downstream, the mean temperature at the centerline increases to ~2000 K at ($X/D_B = 4.0$) (not shown here) for flame HC1, before it decreases further downstream. Similar trends are observed for flame HC2.

Profiles for mean mass fraction of CO_2 and H_2O (not shown) have similar trends to those of the mean temperature. The rms fluctuations of temperatures in flames HC1 and HC2 show peaks that occur at the same radial locations as the mixing layers. The triple peaks in the rms fluctuations of the temperature detected at $X/D_B = 0.9$ are consistent with those observed in methanol flames and overlap with the mixing layers' location.

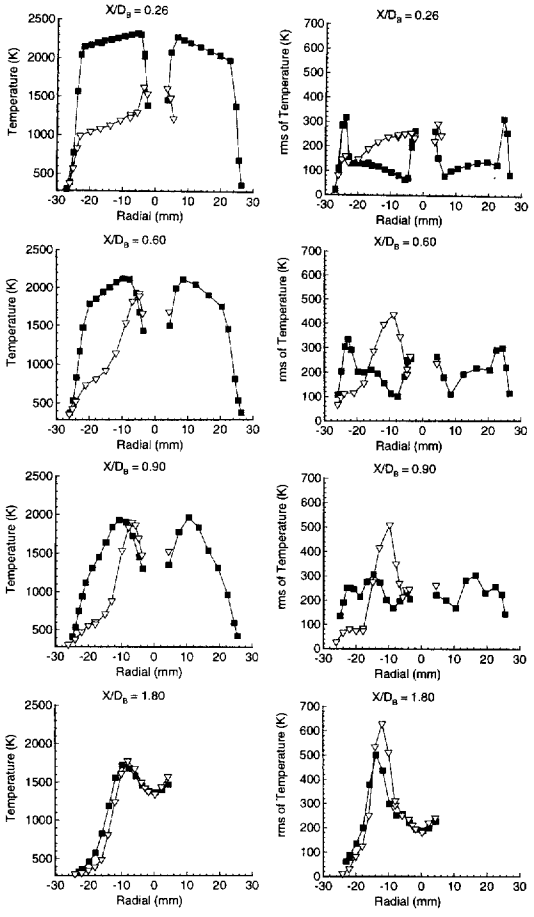

Fig. 15. Radial profiles of mean and rms fluctuations of temperature for different axial locations for H_2/CO flames. Black squares, for HC1 flame; triangles, for HC2 flame.

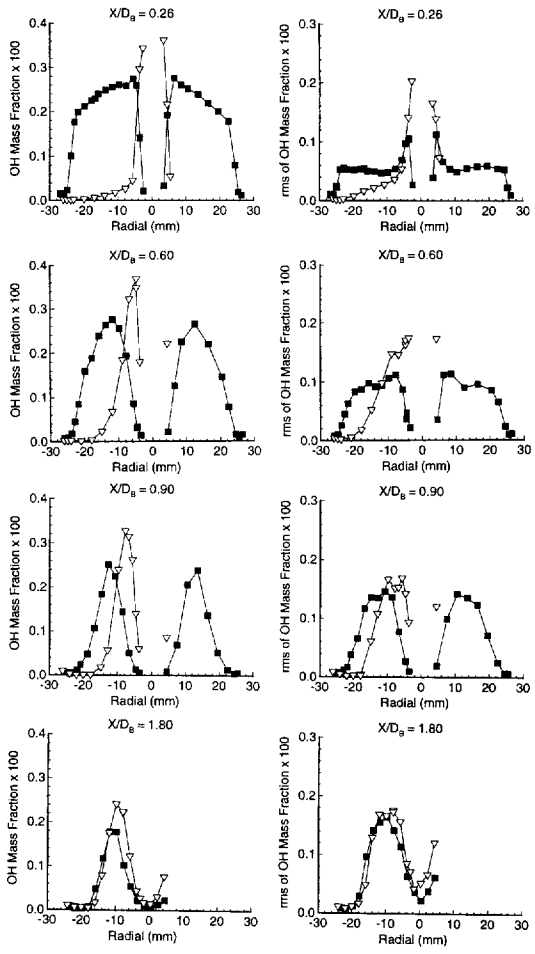

Fig. 16. Radial profiles of mean and rms fluctuations of OH mass fractions for different axial locations of H_2/CO flames. Black squares, for HC1 flame; triangles, for HC2 flame.

Figure 16 shows the mean and rms fluctuations of the OH mass fraction for both flames at locations $X/D_B \leq 1.80$. In this figure, the differences in the burning pattern between flame HC1 and HC2 are most apparent. In flame HC1 the OH levels are high across the whole outer vortex and peak rather on the rich side, whereas in the HC2 flame only a spike of the OH concentration appears at the edge of the inner vortex. Both peaks of OH merge at $X/D_B = 1.8$, where the mixture fraction is similar in both flames. The shift in the OH peak is consistent with visible observation of the recirculation zone where at high jet velocities, the shift of the stoichiometric contour from the outer region to the inner region leads to a nonvisible outer vortex. The rms fluctuations of the OH mass fractions in both flames, exhibit a single peak in the intermediate region in all locations inside the recirculation zone. This is consistent with earlier observations for the CH_3OH flames. The wide reactive zone in the HC1 flame results in a wide rms fluctuations profile for OH covering most of the inner and outer regions.

H_2/CH_4 Flames

Three different flames are presented for this fuel mixture with equal volumes of methane and hydrogen. The flames are HM1 with a jet velocity of 118 m/s, HM2 with 178 m/s, and HM3 with 214 m/s. These flames are at 50, 75, and 91% from extinction, respectively. The addition of

hydrogen to the methane reduces the soot formation substantially and leads to a clean blue recirculation zone. Although the visible length of these flames is $\sim 20 D_B$, measurements are only taken at axial locations extending to $X/D_B = 2.4$. The outer vortex is fully visible in flames HM2 and HM3 and intermittent in flame HM1. In flame HM1, the outer vortex has a nearly uniform rich mixture and the mean stoichiometric contour is located on the outer edge of this vortex. In this region the gradients are very steep and the scalar dissipation rates are high, causing intermittent local extinction at locations close to the burner. Experimentally, the instantaneous data collected in flame HM1 show a bimodal behavior at radial locations $r/R_B > 0.94$ where extinguished parcels of fuel and products can be found. Further downstream in the recirculation zone the mixture fraction gradient is shallower and the bimodality disappears at $X/D_B = 0.9$.

Figure 17 shows mean and rms fluctuations of mixture fraction for axial locations $X/D_B \leq 2.4$ and for the three flames. The mean mixture fraction in the core of the outer vortex in flame HM1 is rich at $\bar{\xi} = 0.16$. The mixture strength in the vortex core decreases with increasing jet velocity and approaches stoichiometric levels for flame HM3. This trend is similar to that found in the H_2/CO and CH_3OH flames discussed earlier. However, at velocities close to extinction the H_2/CH_4 flames still have a slightly rich mixture in their outer vortex, unlike other flames where the mixtures become lean. This is due to mainly the low stoichiometric value for this mixture, which is $\xi_s = 0.05$ compared with $\xi_s = 0.135$ for the other two fuels.

The rms profiles illustrate the same mixing patterns found earlier in CH_3OH and H_2/CO flames. It is apparent, that the rms levels compared at the same axial location are similar for all flames regardless of the fuel. This implies that the mixing pattern in these flames is not affected strongly by the chemistry of the fuel or by finite-rate chemical kinetics.

The temperature profiles plotted for the different flames at the same axial locations as in Fig. 17 show different trends to those for the other fuel mixtures. Close to the bluff-body, flame HM1 has the lowest peak mean temperature of ~1600 K in the outer vortex, which

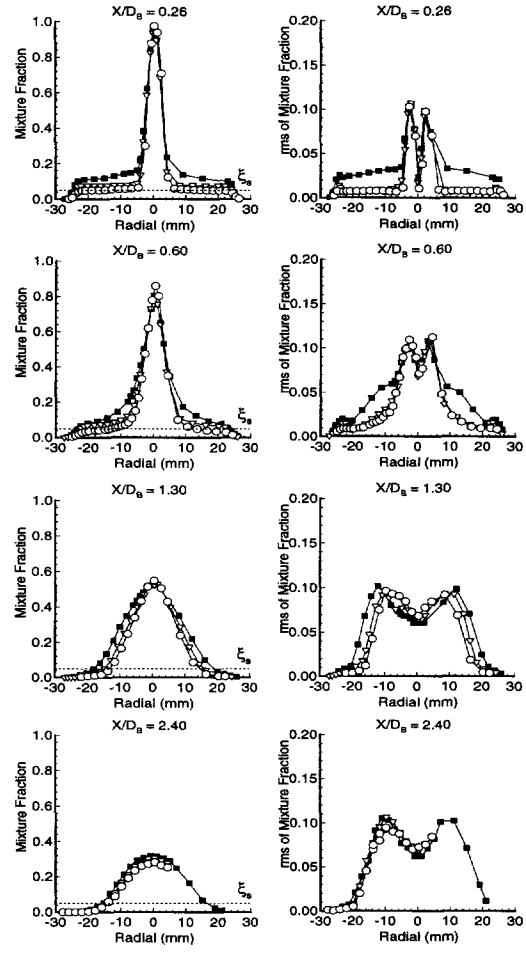

Fig. 17. Radial profiles of mean and rms fluctuations of mixture fraction for different axial locations in H_2/CH_4 flames. Black squares, for HM1 flame; triangles, for HM2 flame; circles, for HM3 flame; and dashed line, for stoichiometric value.

increases to 2000 K further downstream. However, the general trend is for the temperature to decrease when approaching the neck zone in all flames. It is believed though, that the low peak mean temperature found in the recirculation zone of flame HM1 is caused by the averaging of the extinguished and burning parcels at these locations, as discussed earlier. Scatter plots of the temperature at these locations confirm this, as shown in the next section. The rest of the measured scalars show similar trends to those of the CH_3OH and H_2/CO fuel mixtures and are not shown here.

Instantaneous Structure

The instantaneous data are reported here in the form of scatter plots and CPDFs of reactedness. Each of the fuels investigated is considered separately with a range of flames for each fuel. The main focus is on data collected at the neck zone, because it is here that turbulence–chemistry interaction may be most significant and only sample results are given for the recirculation and the reignition zones.

The reporting pattern of the instantaneous data is similar to that for pilot-stabilized flames [27, 28]. This is adequate considering the similarity in the local transient processes that occur locally in both piloted and bluff-body flames, despite differences in the flow pattern. Similar issues regarding the transition to extinction, the deviation of the compositional structure from that of steady laminar flames, and the start of localized extinction are discussed. The results are related and compared with those reported earlier for pilot-stabilized flames, where it was found that even when far from blow-off, the compositional structure may deviate from that computed for steady laminar flames. The measured peak concentration of species like H_2, CO, and OH are higher in varying magnitudes depending on the fuel mixture and the flame condition. The start of LE and the bimodality of the CPDFs as the flames approach extinction are related to simple flame parameters like the stoichiometric mixture fraction ξ_s and the width of the reaction zone $\Delta\xi_R$. A review of the existing data and the findings in these flames can be found in Masri et al. [12].

CH_3OH Flames

Flames ML1, ML2, and ML3, which have jet velocities that are 55, 84, and 95% of that at extinction, respectively, are considered. Figure 18 shows scatter plots for the temperature and percentage mass fractions of CO, CO_2, H_2, H_2O, O_2, OH, and NO (in ppm) for the ML2 flame plotted vs the mixture fraction. The computed structures of steady laminar diffusion flames for methanol also are plotted for three stretch rates a = 5, 100, and 1000 s^{-1}. As mentioned earlier, these calculations were performed with Le = 1.0 and equal species mass diffusivities.

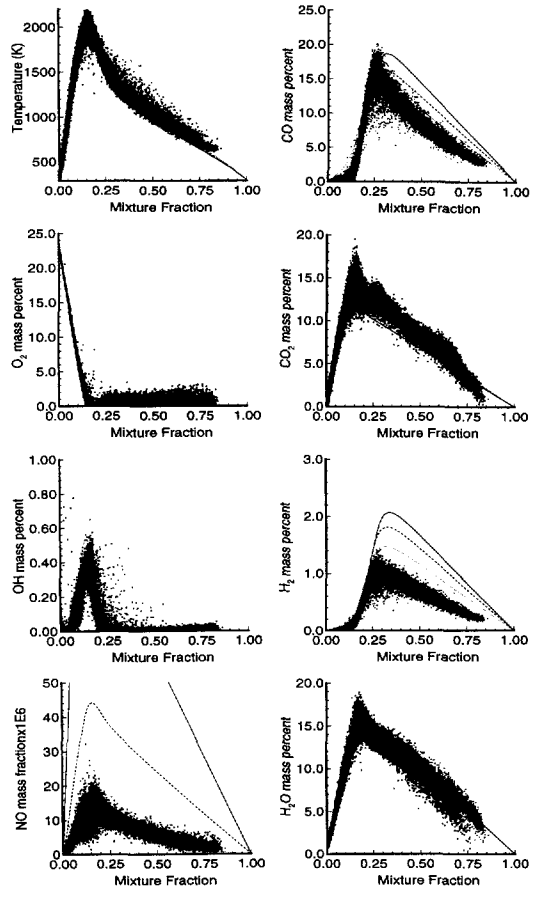

Fig. 18. Scatter plots of temperature and percentage mass fractions of CO, CO_2, H_2, H_2O, O_2, OH, and NO in ppm vs mixture fraction for flame ML2 at axial location X/D_B = 0.6. Solid, dashed, and dotted lines represent computed laminar diffusion flame profiles with constant mass diffusivity and Le = 1.0, for stretch rates a = 5, 100, and 1000 s^{-1}, respectively.

The data in Fig. 18 are collected at axial location X/D_B = 0.6 inside the recirculation zone and at various radial locations across the flame. Most scalars in this figure are similar in trend and magnitude to those calculated for the laminar flames except for CO, H_2, and OH where significant differences are apparent. The peak CO mass fraction is ~0.2, which is slightly higher than that calculated for a laminar flame with a = 5 s^{-1}. The trend for the measured CO data is similar to that calculated for the laminar flames, except in the very rich side of stoichio-

metric where lower values of CO are measured. This also applies to H_2, where the trend of the measurements is very similar to that calculated for the laminar flames, while the peak value is lower than the computed peaks for all stretch rates. The OH radical concentration, on the other hand, is in reasonable agreement with the laminar flame calculations and peaks slightly to the rich side of stoichiometric. The peak NO mass fraction is 20 ppm, which is close to the computed values for the highly stretched laminar flame with $a = 1000\ s^{-1}$. For very rich mixtures with $\xi > 0.5$, the mass fractions of O_2, H_2O, and CO_2 deviate slightly from the expected trend due to strong interferences from the CH_3OH Raman signal. Such interferences are difficult to eliminate entirely in the data processing stages.

Figure 19 shows scatter plots of the same scalars as in Fig. 18, plotted vs the mixture fraction for data collected at axial location $X/D_B = 4.5$, which is in the reignition zone. There is a general agreement here between the turbulent data and the laminar flame calculations. In comparison with the previous figure, the peak OH mass fraction has decreased slightly from 0.58 to ~0.48 while the peak temperature has increased by ~80 K. The CO and H_2 peak percentage mass fractions increased too, from 20 to 24% and from 1.25 to 1.8%, respectively. The peak CO mass fractions are higher than those of the laminar flames, whereas the H_2 mass fractions are bracketed by the profiles computed for flames with low and high stretch rates.

The data presented in Figs. 18 and 19 are for flame ML2, which is relatively close to blow-off ($U_J/U_{BO} = 0.84$). The scatter plots in these figures show no signs of local extinction either in the recirculation or in the reignition zones. This is also true for other methanol flames investigated, as well as for flames of other fuels (H_2/CO and H_2/CH_4). This implies that the fast chemistry assumption may be used to model combustion in these regions of the flames. This will provide adequate predictions for temperature and the major species only. Minor and intermediate species such as CO, H_2, and OH will not be computed correctly using fast chemistry. A model that accounts for finite-rate chemical kinetics is necessary to compute the

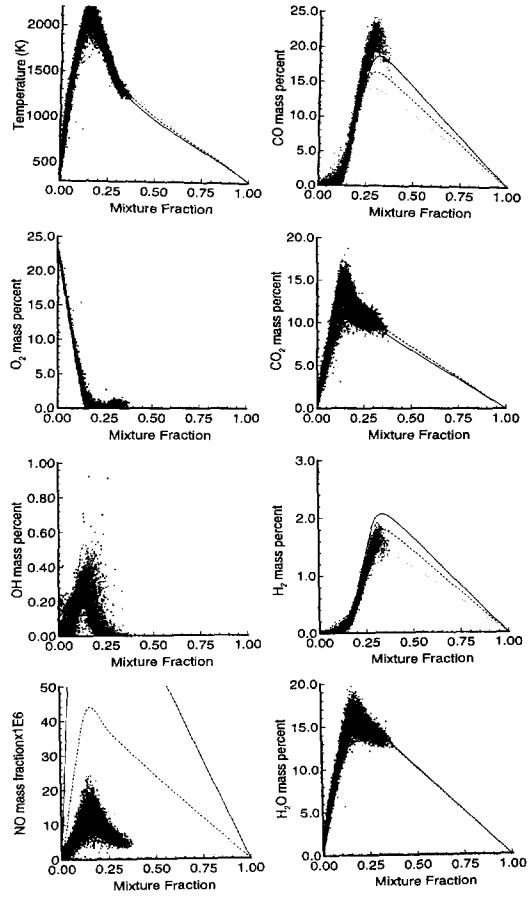

Fig. 19. Scatter plots of temperature and percentage mass fractions of CO, CO_2, H_2, H_2O, O_2, OH, and NO in ppm vs mixture fraction for flame ML2 at axial location $X/D_B = 4.5$. Laminar flame profiles as in Fig. 18.

departure from the steady laminar flame structure observed in Figs. 18 and 19.

Figure 20 shows plots for the same scalars as in Figs. 18 and 19 plotted against the mixture fraction for the ML2 flame. These measurements are collected in the neck zone at axial location $X/D_B = 1.3$ and at different radial locations across the flame. It is evident from this figure that some fluid parcels are either locally extinguished or partially burnt, because the data are spread between the fully burnt and the frozen limits. Extinguished parcels still may have temperatures around 500–800 K due to mixing with the hot products. The percentage OH mass fraction has a peak value of ~0.6%, which is similar to the computed peak value for laminar flames. The CO and H_2 percentage

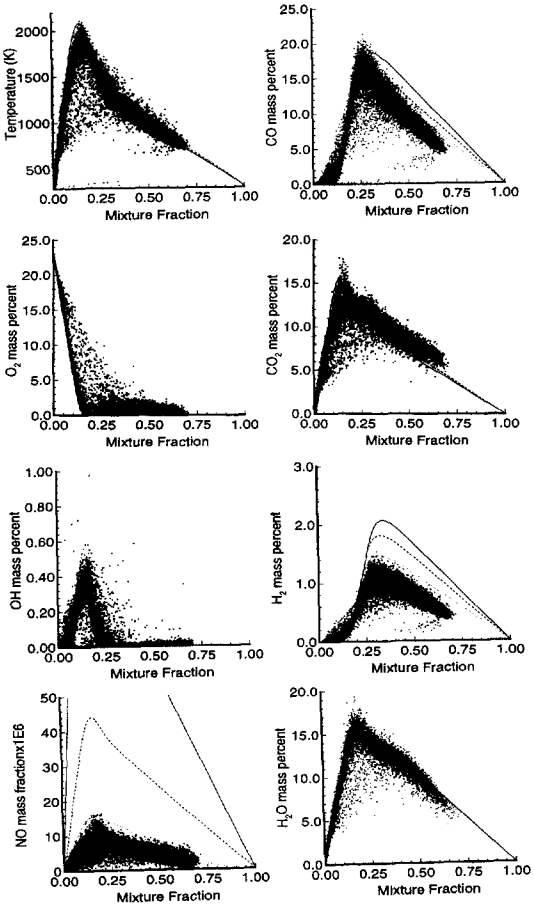

Fig. 20. Scatter plots of temperature and percentage mass fractions of CO, CO_2, H_2, H_2O, O_2, OH, and NO in ppm plotted vs mixture fraction for flame ML2 at axial location X/D_B = 1.3. Laminar flame profiles as in Fig. 18.

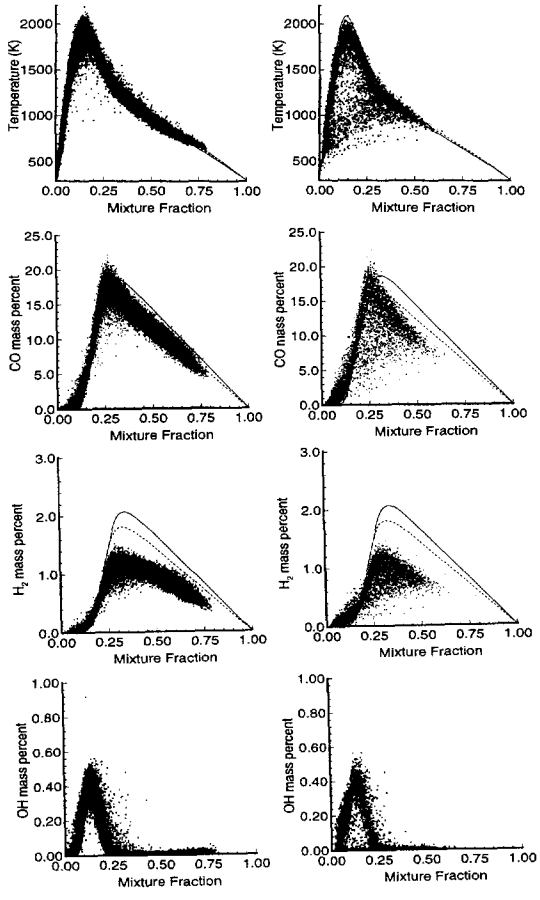

Fig. 21. Scatter plots of temperature and percentage mass fractions of CO, H_2, and OH plotted vs mixture fraction for flames ML1 and ML3 at axial location X/D_B = 1.3. Laminar flame profiles as in Fig. 18.

mass fractions are also similar at 20 and 1.35%, respectively. A drop in the peak NO mass fractions from ~20 ppm at X/D_B = 0.6 to ~16 ppm at this location is observed. This drop is believed to be caused by NO burnout to N_2 [19].

Figure 21 shows scatter plots for the temperature and mass fractions in percent for CO, H_2, and OH for flames ML1 (left column) and ML3 (right column). From the temperature plots in this figure and in Fig. 20, it is apparent that with the increase of the jet velocity the number of extinguished fluid parcels increases and populates the area between the fully burnt and the frozen limits. Also, with the increase of the jet velocity the maximum temperature around stoichiometric mixture fraction drops to 2000 K in flame ML3, whereas the peak temperature is ~2100 K for flame ML1.

Single-point measurements similar to those presented here were reported earlier for piloted [27] and bluff-body [28] stabilized flames of methanol fuel. Super steady flamelet levels of CO were reported for the piloted but not for the bluff-body stabilized flames of methanol. This paper settles this controversy because the peak mass fractions of CO reported in Fig. 19 are indeed in super steady flamelet levels and these are comparable in magnitude to those reported earlier for piloted and bluff-body stabilized flames. It should be noted that the super steady flamelet levels are obtained regardless of the differential diffusion effects on the laminar

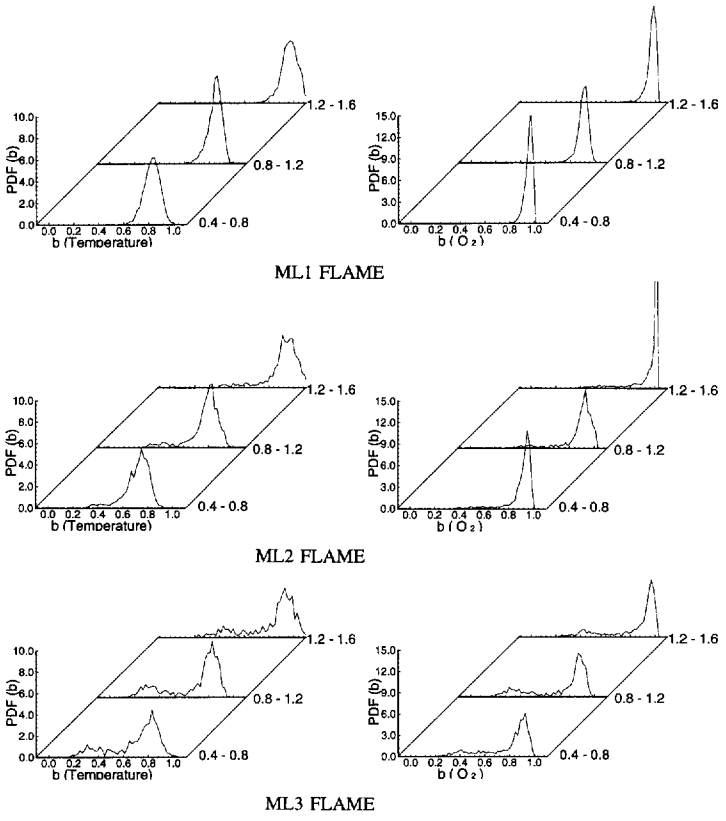

Fig. 22. The PDF of reactedness vs reactedness of temperature and O_2 for three ξ/ξ_s ranges for flames ML1, ML2, and ML3.

flame structure. Peak mass fractions of H_2 are also consistent and are measured at 0.013 both in the pilot- and bluff-body stabilized flames of methanol. This is higher than the peak computed mass fraction for *steady* laminar flames (~0.01) and hence hydrogen was also thought to be in super steady flamelet levels [27, 28]. The computation reported here shows that when constant mass diffusivity is assumed and Le = 1.0, the peak mass fraction of H_2 is computed at 0.02. This puts the peak measured levels of H_2 in both piloted and bluff-body stabilized flames below those computed for laminar flames with Le = 1.0 and hence *not* in super steady flamelet concentration.

The CPDFs of the reactedness determined from the measured temperature and O_2 mass fraction are plotted in Fig. 22 for the methanol flames. The CPDFs for three mixture fraction ratios (lean, stoichiometric, and rich) are shown on each plot. Flame ML1, which is far from blow-off, shows fully reacting CPDFs with a monomodal peak close to $b = 1.0$, whereas in flame ML2 a gradual shift in the CPDF distribution toward lower values of reactedness starts to appear. This indicates that finite-rate chemical kinetic effects are starting to become significant and some fluid samples are reacted partially or extinguished locally. Flame ML3 shows a second peak centered around $b = 0.4$ implying that a significant proportion of fluid samples are now locally extinguished and a distinct bimodal distribution is apparent.

H_2/CO Flames

The three flames considered for this fuel mixture are HC1, HC2, and HC3, with estimated jet velocities of 18, 43, and 74% of that at extinction.

Figure 23 shows scatter plots for temperature and the percentage mass fraction of H_2O, OH, and CO_2 plotted vs the mixture fraction for flames HC1 and HC3. These data are taken at the axial location $X/D_B = 1.8$, which falls in the neck zone of both flames. Laminar diffusion flames computed for stretch rates $a = 5$, 100, 8000 s^{-1} are plotted along with the turbulent

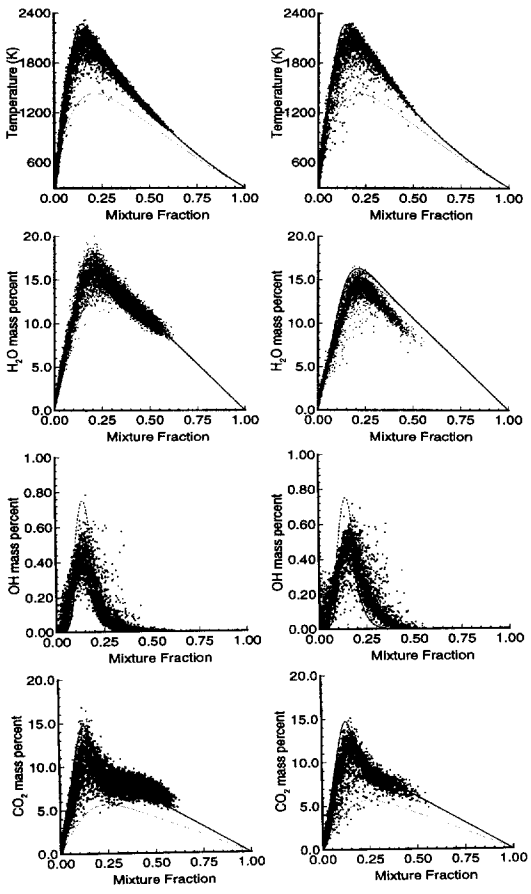

Fig. 23. Scatter plots of temperature and percentage mass fractions of H_2O, OH, and CO_2 plotted vs mixture fraction for flames HC1 and HC3 at axial location $X/D_B = 1.8$. Solid, dashed, and dotted lines represent computed laminar diffusion flame profiles with constant mass diffusivity and Le = 1.0, for stretch rates $a = 5$, 100, and 8000 s^{-1}, respectively.

data for each of the scalars. The turbulent data is bracketed by the calculations for the fully stretched and fully burnt cases.

It is apparent that there is no sign of any LE for any of the scalars even for the HC3 flame, which has a velocity 74% of that at extinction. This is most obvious in the OH plots where all samples around the reaction zone have values that are non-zero. It was not possible to conduct experiments with higher jet velocity because of the extreme noise and limitations of the equipment. However, the results are consistent with previous observations by Masri et al. [42] for pilot-stabilized flames. Flames of H_2/CO fuel mixtures have broad reaction zones that generally lead to a delay in the start of local extinction. This issue is discussed later.

Figure 24 shows the CPDFs of the reactedness determined from the measured temperature and O_2 mass fraction for the HC1, HC2, and HC3 flames. The CPDFs for the two scalars are monomodal in all flames and are centered around $b \sim 1.0$, implying that the H_2/CO flames are still fully reacting and do not show any sign of localized extinction. As the jet velocity is increased the tails of the CPDFs gradually move to lower values of reactedness, indicating that fluid samples are departing from the fully burnt limit. The strain rates are not high enough, however, for local extinction to occur.

H_2/CH_4 Flames

For this fuel mixture the addition of H_2 to the CH_4 broadens the reaction zone only slightly and $\Delta\xi_R$ increases from 0.08 for pure methane to 0.091 for this fuel mixture. The three flames considered are HM1, HM2, and HM3, with velocity ratios of 50, 75, and 91% of those at extinction, respectively.

Figure 25 shows scatter plots of temperature and percentage mass fractions of selected species plotted against the mixture fraction for the HM1 flame. These measurements are taken at an axial location $X/D_B = 1.8$ and include several radial locations across the flame. The laminar flame calculations for this fuel mixture are plotted for stretch rates of $a = 5$, 100, and 1400 s^{-1}. Temperature and most reactive scalars generally lie within, or close to, the envelope of the laminar flame calculations. Significant deviations, however, exist for CO where the peak measured level reaches an unrealistic mass fraction of 25% at $\xi \sim 0.1$. This is the region where the fluorescence interference is at its worst. The CO signal is most affected by these interferences, which are believed to be caused by, primarily, C_2 fluorescence. Discounting these effects, the peak CO level in these flames is believed to be in super steady flamelet levels. The peak OH level, however, is similar to that computed for steady laminar diffusion flames. This is inconsistent with measurements reported for piloted flames of CH_4 showing peak levels of OH in super steady flamelet

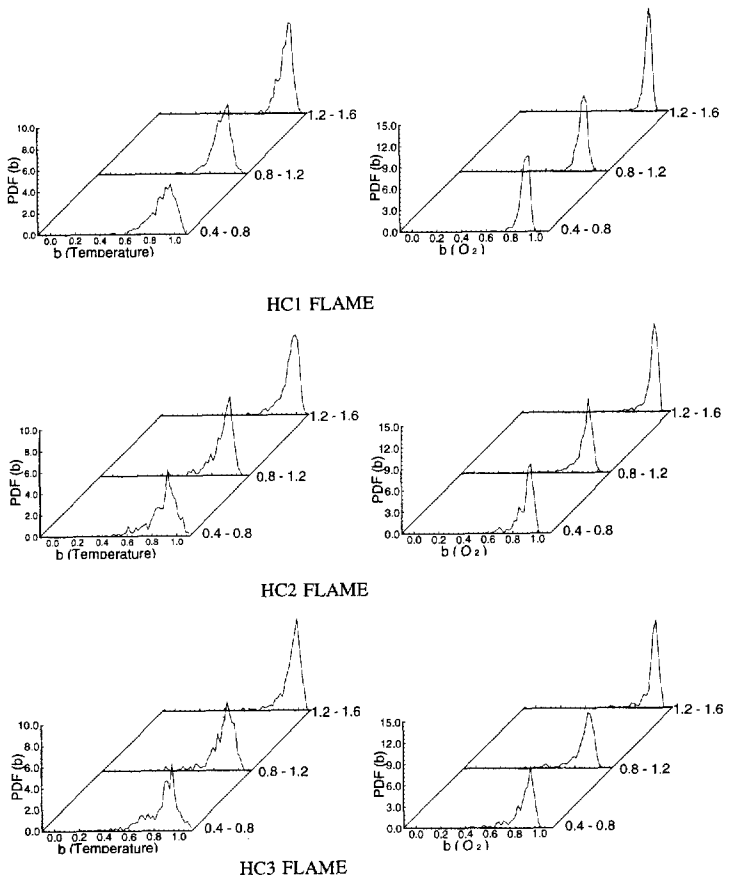

Fig. 24. PDF of the reactedness vs the reactedness of temperature and O_2 for three ξ/ξ_s ranges for flames HC1, HC2, and HC3.

concentrations [43]. The hydrogen content in this fuel mixture is much higher than that of the piloted flame investigated earlier and this may cause a decrease in the peak levels of OH.

Figure 26 shows temperature and percentage mass fractions of H_2O, OH, and CO_2 plotted against the mixture fraction for the HM2 and HM3 flames. As for the methanol flames (Figs. 20–21), the temperature plots show an increase in the number of locally extinguished samples with increase in the fuel-jet velocity. Similar behavior is observed in the other reactive scalars. Flame HM2 has a velocity ratio of 75% and already shows significant signs of local extinction. This is consistent with results reported earlier for piloted flames. A quantitative measure of the proportion of the extinguished samples is introduced later in the Discussion Section.

Figure 27 shows the CPDFs of reactedness determined from the measured temperature and O_2 mass fraction for the H_2/CH_4 flames. In this figure, flame HM1 shows a wider CPDF distribution than any of the other flames with the same velocity ratio of $U_J/U_{BO} = 0.5$. For flame HM2 with $U_J/U_{BO} = 0.75$ the CPDFs of both b_T and b_{O_2} are broad, implying that a significant proportion of fluid samples are either partially burnt or locally extinguished. Flame HM3 shows a clear bimodal distribution of the CPDF for both O_2 and temperature, as seen too in the scatter plots of Fig. 26. The early start of LE is a characteristic of these flames.

DISCUSSION

Mean Structure

In these flames and mainly in the jet dominant "configuration," the momentum flux of the jet has a strong influence on the structure of the

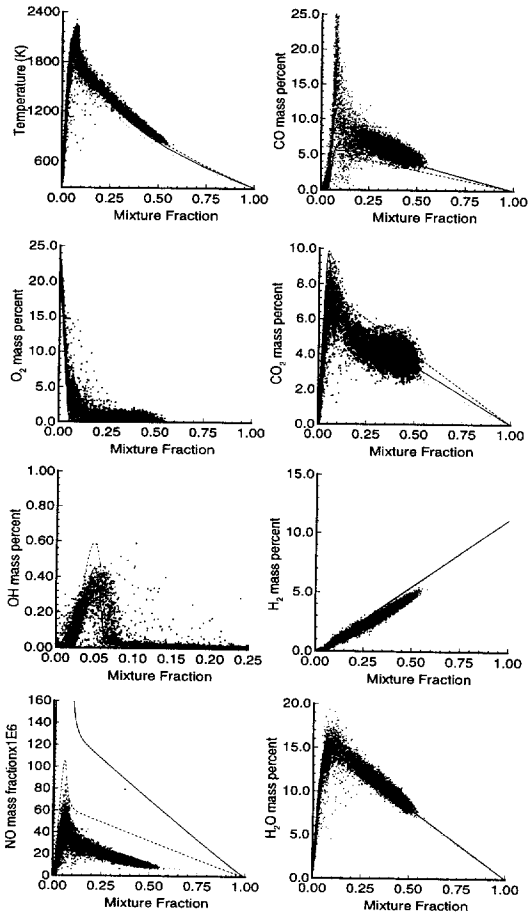

Fig. 25. Scatter plots of temperature and percentage mass fractions of CO, CO_2, H_2, H_2O, O_2, OH, and NO in ppm vs mixture fraction for flame HM1 at axial location X/D_B = 1.8. Solid, dashed, and dotted lines represent computed laminar diffusion flame profiles with constant mass diffusivity and Le = 1.0, stretch rates a = 5, 100, and 1400 s^{-1}, respectively.

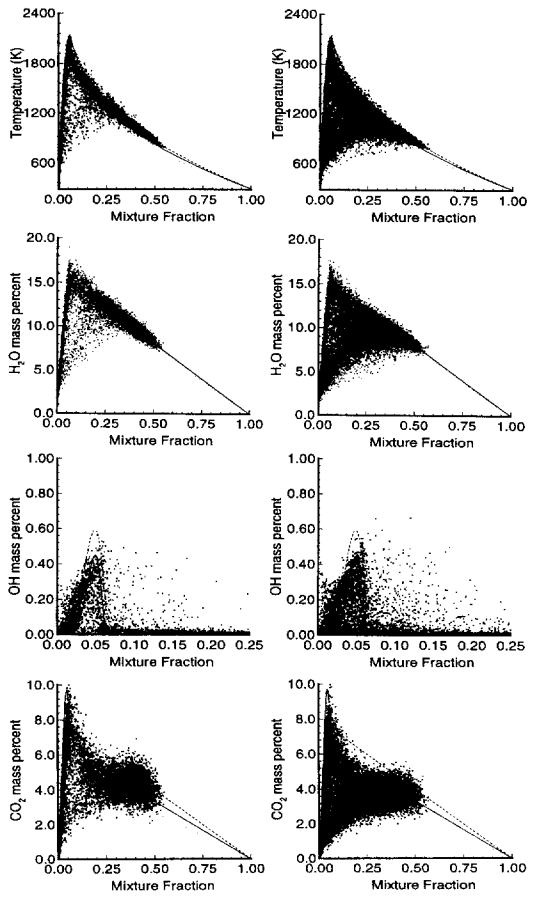

Fig. 26. Scatter plots of temperature and percentage mass fractions of H_2O, OH, and CO_2 vs the mixture fraction for flames HM2 and HM3 at axial location X/D_B = 1.8. Laminar flame profiles as in Fig. 25.

recirculation zone. Regardless of the fuel, three mixing layers exist within the recirculation zone. The relative strength and contribution to overall mixing in each of these layers depend on the coflow and fuel-jet velocities and on the location of the shear layers. Velocity measurements in these flows [44] reveal two shear layers in the recirculating region. The first is the inner layer, between the inner vortex and the fuel jet; the second is the outer layer in the outer edge of the outer vortex. At these locations the velocity fluctuations mainly in the dominant axial component is the highest. The position of the mixing layers relative to the shear layers is not resolved fully yet. However, from the data presented here and from preliminary flow field data, it is apparent that there is some correlation between the outer and inner mixing layers and the shear layers. This interaction affects the intensity of the fluctuations of the reactive scalars.

Also it is found that a consistent drop in the mixture strength of the outer vortex core occurs with increase in the fuel-jet velocity. At intermediate jet velocities, the reaction zone lies closer to the outer edge of the outer region, while the core of the outer vortex remains fuel rich on average. At higher jet velocity the outer vortex becomes leaner and the reaction zone shifts inward, closer to the jet. For fuels with low stoichiometric mixture fractions, such as the

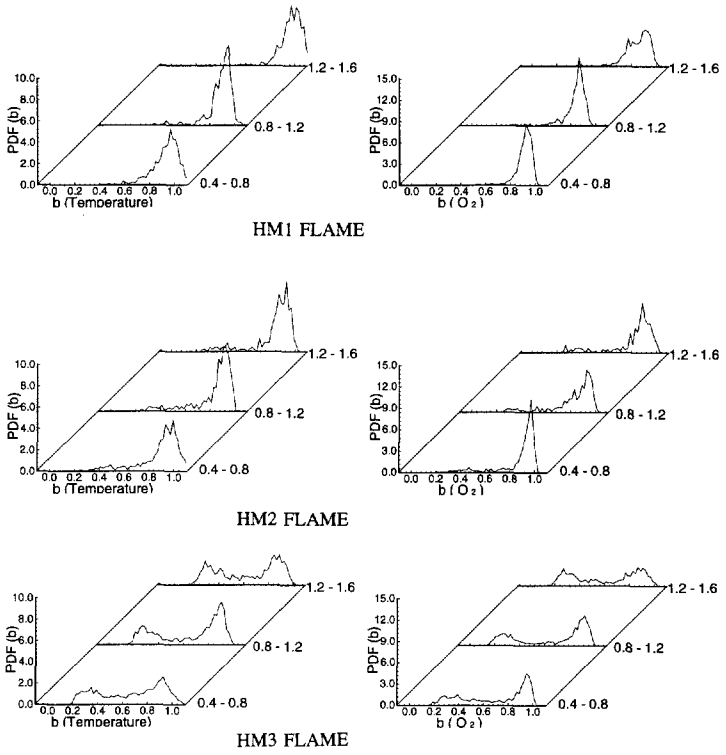

Fig. 27. The PDF of reactedness vs reactedness of temperature and O_2 for three ξ/ξ_s ranges for flames HM1, HM2, and HM3.

H_2/CH_4 flames, the mixture in the outer vortex remains rich even at jet velocities close to extinction. Also apparent is that the flow field influences the location of the stoichiometric mixture fraction contour relative to the two vortices identified in this zone, and this leads to the structural differences in the recirculation zones.

To contrast the mixing characteristics of the different flames, the mean centerline mixture fraction ($\bar{\xi}_{cl}$) is plotted against the normalized distance above the burner in Fig. 28. Three important points can be noted:

1. Downstream of the recirculation zone the decay rate of $\bar{\xi}_{cl}$ for the same fuel mixture is similar, regardless of the fuel-jet velocity and hence finite-rate chemistry effects. Inside the recirculation zone, however, a small difference can be found in $\bar{\xi}_{cl}$ between the highest and lowest velocity flames.
2. The decay rate of $\bar{\xi}_{cl}$ downstream of the recirculation zone scales inversely with (X/D_B), as to be expected in ordinary jet flames. This illustrates the similarities between the spread rate of the bluff-body flames above the recirculation zone and that of an ordinary jet flame.

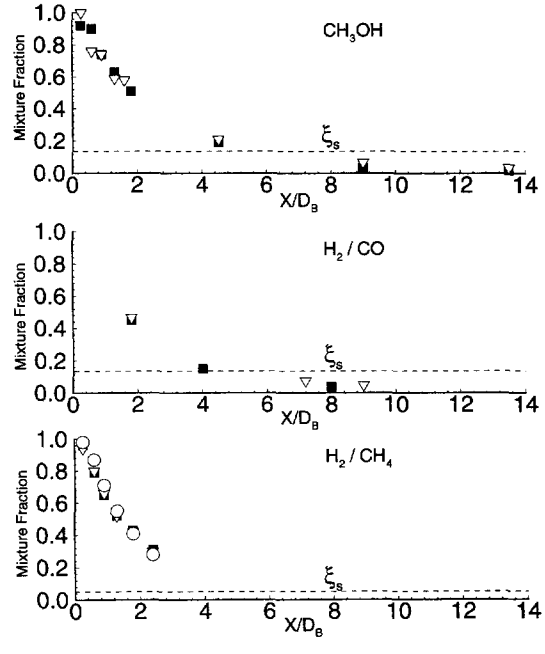

Fig. 28. Axial profiles of mean mixture fraction at the centerline for all flames. Black squares, for ML1, HC1, and HM1 flames; triangles, for ML2, HC2, and HM2 flames; circles, for HM3 flame; dotted lines, stoichiometric values.

3. The overall decay rate of $\bar{\xi}_{cl}$ is highest in the H_2/CH_4 and lowest for the CH_3OH flames.

The difference in the mixture strength has large effects on the production of various species and on the burning pattern inside the recirculation zone. Flames such as ML2, HC1, and HM3 have outer vortices with mixture fraction levels that are close to stoichiometric. In these flames the reactive zone is broad, covering almost the full width of the bluff-body. In other flames, the mixture in the outer vortex is either too rich or too lean. Reaction occurs then in a thin strip either at the outer edge of the large vortex or close to the inner vortex depending on where the stoichiometric mixture fraction lies. The recirculation zone structure has minor effects on the overall flame structure further downstream and this is consistent with earlier results reported for NO [19].

The mean mixture fraction within the core of the outer vortex $\bar{\xi}_{vo}$ depends not only on U_J and U_{CO} but also on the diameter ratio D_B/D_J and on the heat release rate of the fuel used and hence the density ratio. There are not enough data to produce a correlation between $\bar{\xi}_{vo}/\xi_s$, D_B/D_J, U_J/U_{CO}, and ρ_J/ρ_{CO} but preliminary plots for the flames studied here have shown that there is a definite negative correlation between $\bar{\xi}_{vo}/\xi_s$ and U_J/U_{CO}. Many more cases need to be studied to produce a more convincing correlation relating all the foregoing parameters. In the recirculation zone, scatter plots of reactive species show that there is no major effects of the finite-rate chemistry and the fast chemistry assumption can be used to model the temperature and the major species. Further downstream of the recirculation zone, the structure of the flames are similar to those of streaming jets. In the neck zone, the flame blows off at high enough velocities and chemical effects are high.

Instantaneous Structure

Deviation from the computed steady laminar flame structure has been observed for intermediate species such as H_2, CO, and OH in both piloted and bluff-body stabilized flames. This may be caused by transient effects that exist in turbulent flames due to concentration fluctuations as well as differential diffusion effects that may be more relevant in laminar flame calculations. Barlow and Chen [38] have investigated this issue computationally and concluded that the sudden decrease of the scalar of dissipation rate in a fully burning laminar flame can cause the overshoot of intermediate species such as CO and OH. Furthermore, they pointed out that the effects of differential diffusion can be very substantial in these calculations and may lead to discrepancies between the turbulent and the calculated steady laminar flame data. Mauss et al. [39] have shown that for unsteady laminar flames the reignition of an extinguished sample also leads to higher CO values compared with steady laminar flames with the same stretch rates.

The hydroxyl radical shows some inconsistency in that the peak levels reported earlier for piloted flames [27, 40, 42] are higher than those measured for somewhat similar fuels. The reasons for this are not fully understood and may be partly caused by the effects of the pilot or by different turbulence levels in the flames.

The bimodal behavior of flames as they approach extinction is a feature that depends on the fuel mixture. Masri et al. [12] used a bimodality factor B proposed by Atkinson [41] to quantify the bimodality distribution of the PDF. This factor is defined as

$$B_i = k_i - s_i^2 \tag{4}$$

where k_i is the kurtosis and s_i is the skewness of the PDF calculated for species i. With this definition for $B_i = 1.0$ the PDF has a double delta function distribution, whereas for $B_i = 3.0$ the distribution is Gaussian.

The lowest bimodality factors computed for temperature, CO_2, O_2, and H_2O for the various flames at the axial locations and mixture fraction ranges plotted earlier, are shown in Table 3. For flames with CH_3OH and H_2/CH_4 fuels, the $\bar{B}_i$ factors from the three mixture fraction ranges decrease with increase of fuel-jet velocity and show a tendency toward a bimodal distribution when approaching extinction. However, for the H_2/CO flames there is no consistent trend for all scalars, and $\bar{B}_T$ and $\bar{B}_{H_2O}$ for flame HC1 show nearly Gaussian distributions of the CPDFs. Also included in this table is the width

TABLE 3

Width of Reaction Zone and Start of LE Results for Present Bluff-Body and Previous Piloted Stabilized Nonpremixed Turbulent Flames

Flame	$\Delta\xi_R$	$\xi_s/\Delta\xi_R$	$\bar{B}_T$	B_{CO_2}	$\bar{B}_{O_2}$	B_{H_2O}	Expected ($\bar{B}_{min}$)	Expected (LE)
ML1	0.256	0.527	3.91	3.13	9.53	2.94	1.35–1.45	0.67–0.70
ML2			3.08	2.76	2.76	3.70		
ML3			1.54	1.86	1.46	1.80		
HC1	0.315	0.428	3.00	2.55	3.68	3.00	1.34–1.40	0.79–0.82
HC2			3.26	2.68	3.15	3.42		
HC3			3.07	2.65	3.98	3.65		
HM1	0.091	0.549	4.19	3.34	4.96	4.25	1.42–1.46	0.63–0.66
HM2			2.29	2.54	2.11	2.25		
HM3			1.40	1.63	1.33	1.43		

$\Delta\xi_R$ is the width of the reaction zone, $\bar{B}_i$ is the averaged minimum bimodality factor calculated for scalar i, $\bar{B}_{min}$ is the averaged minimum bimodality factor expected for this $\xi/\Delta\xi_R$ according to Ref. 12. The LE is the U_J/U_{BO} threshold value where LE starts according to Ref. 12.

of the reaction zone ($\Delta\xi_R$) for the different fuel mixtures. This is determined from steady laminar diffusion flame calculations as the average width in mixture fraction space where the formation rates of H_2O, CO_2, and OH exceed 10% of their maximum value for a range of stretch rates.

In an extensive analysis of the structure of turbulent piloted flames of a range of fuels, Masri et al. [12] have generated diagrams that characterize the behavior of the flames approaching blow-off with respect to simple parameters like ξ_s and $\Delta\xi_R$. The start of the LE and the bimodality factor were correlated with respect to $\xi_s/\Delta\xi_R$. It was found that the LE decreases with increase of $\xi_s/\Delta\xi_R$, whereas the minimum averaged bimodality factor $\bar{B}_{min}$ shows an opposite trend and a positive correlation. For the flames investigated here, and using such diagrams, the expected range of value of LE and $\bar{B}_{min}$ are tabulated in Table 3. The minimum $\bar{B}_i$ factors computed from the bluff-body flame data are in agreement with the expected values, except for the H_2/CO flames where the jet velocities were far from extinction due to experimental limitations. The expected start of LE also is consistent with the current results. The CH_3OH and the H_2/CH_4 flames are expected to start showing local extinction at velocity ratios of 68 and 64%, respectively. The scatter plots presented here for flames ML1 and HM1 (55 and 50%), respectively, show no signs of LE. Flames of H_2/CO fuel, are expected to start extinguishing locally at $U_J/U_{BO} = 80\%$. This explains why flames like HC1, HC2, and HC3, which have jet velocities that are 18, 43, and 74% of that at extinction, do not show any sign of LE.

CONCLUSIONS

1. Three mixing layers are identified in the recirculation zone; an outer layer between the outer vortex and the air coflow, an intermediate layer between the outer vortex and the inner vortex, and an inner layer between the inner region and the fuel jet. The relative contribution of each layer to the overall mixing varies with the fuel and jet velocity.
2. The increase in the fuel-jet momentum flux decreases the strength of the mixture in the outer vortex and at a sufficiently high jet velocity the stoichiometric mixture fraction contour shifts from the outer region to the inner region of the recirculation zone. This in turn shifts the reaction zone toward the fuel jet and leaves only combustion products in the outer vortex.
3. The effect of the reaction zone shift on the temperature and mean OH radial profiles is only apparent inside the recirculation zone. Profiles at locations further downstream in the jet-like part of the flame are not affected strongly.
4. The decay rate of the mixture fraction on the centerline and downstream of the recircula-

tion zone exhibits a similar trend to that observed in an ordinary jet flame. Different decay trends are found inside the recirculation zone.

5. The computed structure of steady laminar diffusion flames is significantly affected by differential diffusion of species. It was found that calculations with equal mass diffusivities and Le = 1.0 are more a appropriate guide for the data presented here especially for temperature and stable species such as CO_2 and H_2O.
6. The measured temperature and stable species mass fractions in the recirculation zones as well as the reignition zones of all flames studied are very close to the fully burnt limits computed for steady laminar diffusion flames. This implies that the fast chemistry assumption may be used to simulate the structure of these regions in the flames.
7. For a given fuel mixture, peak mass fractions of CO and H_2 are similar for both piloted and bluff-body burners. Peak measured concentration of CO may be in super steady flamelet concentration whereas peak measured H_2 is found to be within steady flamelet levels if calculated with equal mass diffusivities and Le = 1.0.
8. The peak measured mass fractions of OH are lower than those reported earlier for piloted stabilized flames of similar fuels. Also, OH is found not to be in super steady flamelet concentration in these flames. The reason for this discrepancy partly may be caused by the pilot and this issue needs further investigation.
9. The LE for bluff-body stabilized flames of methanol and H_2/CH_4 fuels start at $U_J/U_{BO} \approx 68$ and 64%, respectively. The start of LE as well as the extent of the bimodality of the CPDFs as the flames approach blow-off, are consistent with results reported earlier for piloted flames.

The authors acknowledge the support of the Australian Research Council and the United States Department of Energy, Office of Basic Energy Sciences, Division of Chemical Sciences.

REFERENCES

1. Masri, A. R., Data-base available from *Mechanical and Mechatronic Engineering*, The University of Sydney, NSW, 2006, Australia. (http://www.me.su.oz.au/research/energy/energy.html).
2. Warnatz, J. (1981). *Eighteenth Symposium (International) on Combustion*, The Combustion Institute, Pittsburgh, pp. 369–384.
3. Westbrook, C. K., and Dryer, F. L., *Combust. Sci. Technol.* 20:125–141 (1979).
4. Miller, J. A., Smooke, M. D., Green, R. M., and Kee, R. J., *Combust. Sci. Technol.* 34:149–177 (1983).
5. GRI Mechanism 2.1, available from the World Wide Web cite *http://www.gri.org.*
6. Smooke, D. M., Ed., *Reduced Kinetic Mechanisms and Asymptotic Approximations for Methane-Air Flames*, Springer-Verlag, 1990.
7. Peters, N., and Rogg, B., Eds., *Reduced Kinetics Mechanisms for Applications in Combustion Systems*, Springer-Verlag, 1992.
8. Bilger, R. W., *Physics of Fluids* A5(2):436–444 (1993).
9. Peters, N. (1986). *Twenty-First Symposium (International) on Combustion*, The Combustion Institute, Pittsburgh, pp. 1231–1250.
10. Pope, S. B., *Prog. Energy Combust. Sci.* 11:119–192 (1985).
11. Menon, S., Calhoon, W. H., Jr., and Goldin, G. (1994). *Twenty-Fifth Symposium (International) on Combustion*, The Combustion Institute, Pittsburgh, pp. 1125–1131.
12. Masri, A. R., Dibble, R. W., and Barlow, R. S., *Prog. Energy Combust. Sci.* 22:307–362 (1996).
13. Roquemore, W. M., Bradley, R. P., Stutrud, J. S., Reeves, C. M., Obringer, C. A., and Britton, R. L., *Utilization of Laser Diagnostics to Evaluate Combustor Models*, AGARD Propulsion and Energies Panel, Cesme, Turkey, 1983, pp. 1–20.
14. Roquemore, W. M., Bradley, R. P., Stutrud, J. S., Reeves, C. M., and Britton, R. L. (1983). AIAA *21st Aerospace Science Meeting*, Paper AIAA 83-0335, Reno, NV.
15. Prade, B., and Lenze, B. (1992). *Twenty-Fourth Symposium (International) on Combustion*, The Combustion Institute, Pittsburgh, 1992, pp. 369–375.
16. Masri, A. R., and Bilger, R. W. (1984). *Twenty Symposium (International) on Combustion*, The Combustion Institute, Pittsburgh, pp. 319–320.
17. Masri, A. R., Dally, B. B., Barlow, R. S., and Carter, C. D. (1994). *Twenty-Fifth Symposium (International) on Combustion*, The Combustion Institute, Pittsburgh, pp. 1301–1308.
18. Correa, S. M., and Gulati, A., *Combustion and Flame* 89:195–213 (1992).
19. Dally, B. B., Masri, A. R., Barlow, R. S., Fiechtner, G. J., and Fletcher, D. F. (1996). *Twenty-Sixth Symposium (International) on Combustion*, The Combustion Institute, Pittsburgh, Vol. 2, pp. 2191–2197.
20. Schefer, R. W., Namazian, M., and Kelly, J., *Combust. Sci. Technol.* 56:101–138 (1987).
21. Namazian, M., Schefer, R. W., and Kelly, J., *AIAA*

27th Aerospace Science Meeting, Paper AIAA 89-0058 (1989), Reno, NV.
22. Dally, B. B., Fletcher, D. F., and Masri, A. R. (1995). *Proc. First Asian CFD Conference*, Hong Kong, pp. 177–182.
23. Dally, B. B., Masri, A. R., and Fletcher, D. F. (1995). *Twelfth Australasian Fluid Mechanics Conference*, Sydney, Australia, Vol. 1, pp. 529–532.
24. Grinstein, F. F., and Kailasanath, K., *Combustion and Flame*, 100:2–10 (1995).
25. Correa, S. M., and Pope, S. B. (1992). *Twenty-Fourth Symposium (International) on Combustion*, The Combustion Institute, Pittsburgh, pp. 279–285.
26. Masri, A. R., Subramanian, S., and Pope, S. B. (1996). *Twenty-Sixth Symposium (International) on Combustion*, The Combustion Institute, Pittsburgh, Vol. 1, pp. 49–57.
27. Masri, A. R., Dibble, R. W., and Barlow, R. S., *Combustion and Flame* 89:167–185 (1992).
28. Masri, A. R., Dibble, R. W., and Barlow, R. S. (1992). *Twenty-Fourth Symposium (International) on Combustion*, The Combustion Institute, Pittsburgh, pp. 317–324.
29. Barlow, R. S., Fiechtner, G. J., and Chen, J.-Y. (1996). *Twenty-Sixth Symposium (International) on Combustion*, The Combustion Institute, Pittsburgh, Vol. 2, pp. 2199–2205.
30. Nguyen, Q. V., Dibble, R. W., Carter, C. D., Fiechtner, G. J., and Barlow, R. S., *Combustion and Flame* 105:499–510 (1996).
31. Bilger, R. W., *Combustion and Flame* 80:135–149 (1990).
32. Eckbreth, A. C., *Laser Diagnostics for Combustion Temperature and Species*, (A. K. Gupta, and D. G. Lilley, Eds.), Gordon and Breach, U.K., 1987.
33. Barlow, R. S., and Carter, C. D., *Combustion and Flame* 97:261–280 (1994).
34. Mansour, M. S., Bilger, R. W., and Dibble, R. W., *Combustion and Flame* 82:411–425 (1990).
35. Kerstein, A. R., Cremer, M. A., and McMurtry, P. A., *Phys. Fluids* 7:1999–2007 (1995).
36. Smith, L. L., Dibble, R. W., Talbot, L., Barlow, R. S., and Carter, C. D. (1993). *31st Aerospace Science Meeting and Exhibit*, AIAA-93-0804, Reno, NV.
37. Chen, R-H, Driscoll, J. F., Kelly, J., Namazian, M., and Schefer, R. W., *Combust. Sci. Technol.* 71:197–217 (1990).
38. Barlow, R. S., and Chen, J.-Y. (1992). *Twenty-Fourth Symposium (International) on Combustion*, The Combustion Institute, Pittsburgh, pp. 231–237.
39. Mauss, F., Keller, D., and Peters, N. (1990). *Twenty-Third Symposium (International) on Combustion*, The Combustion Institute, Pittsburgh, pp. 693–698.
40. Starner, S. H., Bilger, R. W., Dibble, R. W., and Barlow, R. S. (1990). *Twenty-Third Symposium (International) on Combustion*, The Combustion Institute, Pittsburgh, pp. 645–651.
41. Atkinson, J. D., Department of Mechanical and Mechatronic Engineering The University of Sydney, NSW, Australia, Personal communication, 1984.
42. Masri, A. R., Bilger, R. W., and Dibble, R. W., *Combustion and Flame* 81:260–276 (1990).
43. Masri, A. R., Bilger, R. W., and Dibble, R. W., *Combustion and Flame* 73:261–285 (1988).
44. Dally, B. B., Fletcher, D. F., and Masri, A. R., *Combustion Theory and Modelling*, in press.

Received 31 May 1996; accepted 6 September 1997